



Research Paper

Experimental and computational study on utilising graphene oxide for adsorption cooling and water desalination

Handsome Banda^a, Ahmed Rezk^{a,*}, Eman Elsayed^b, Ahmed Askalany^c

^a Energy and Bio-products Research Institute (EBRI), College of Engineering and Physical Science, Aston University, Birmingham B4 7ET, UK

^b School of Mechanical Engineering, University of Birmingham, Birmingham B15 2TT, UK

^c Mechanical Department, Faculty of Technology and Education, Sohag University, Sohag 82524, Egypt

ARTICLE INFO

Keywords:

Graphene oxide
Silica gel
Exergy analysis
Adsorption cooling
Desalination

ABSTRACT

The adsorbent material's thermal and sorption characteristics are the critical criteria that affect the adsorption systems' overall performance. Therefore, this paper experimentally and computationally studies the utilisation of graphene oxide of a few atomic layers as a parent adsorbent material owing to its reported high thermal performance potential. Graphene oxide performance was benchmarked against the widely investigated silica gel adsorbent, emphasising adsorption cooling cum desalination application as the most needed to address the lack of sustainable cooling and clean water scarcity. Quantitative and qualitative analyses were undertaken to determine the influence of the evaporator temperature, cycle time and heat source temperature on the material and system levels. The results showed that graphene oxide enhances thermal performance by 44% compared to silica gel and adsorption by up to 57%. Furthermore, graphene oxide, compared to silica gel as a parent adsorbent, enhanced the system's specific daily water production by up to 44.4%, the specific cooling power by up to 29.5%, the coefficient of performance by up to 17.2% and the exergy efficiency by up to 15.8%.

1. Introduction

The increasing water scarcity has resulted in over 2 billion people not having access to fresh water supplies globally [1]. Therefore, there has been an increasing demand for brackish and seawater desalination to alleviate such challenges [2]. More interestingly, most societies facing water scarcity also face high temperatures and require sustainable cooling for comfort and food preservation [3]. Like conventional water desalination systems (e.g., Multi-effect desalination, reverse osmosis and multistage flash), vapour compression cooling systems are energy intensive. Moreover, the vapour compression systems utilise refrigerants that have long-lasting adverse environmental impacts, such as hydrochlorofluorocarbon (HCFC) and Chlorofluorocarbon (CFC) [4]. In addition, the increasing energy consumption for cooling raises major environmental concerns related to energy production and thermal pollution [3,5]. Therefore, using environmentally friendly refrigerants, such as water, methanol and ethanol, and the ability to utilise low-grade waste and renewable heat makes the adsorption system the most feasible alternative to conventional desalination and cooling systems [6–9].

Low heat and mass transfer in the current adsorption beds – the core component in adsorption systems – lead to low energy conversion

efficiency, hence poor clean water and cooling production [9–11]. Most recorded studies on adsorption systems focussed on enhancing the adsorption system performance by applying new adsorbents, adsorbent-bed heat exchange designs and adsorption cycle layouts [12–14]. However, the poor heat transfer at the material level remains challenging.

Conventional adsorbents, such as silica gel and zeolite, have limited adsorption capacity and poor thermal characteristics [15,16]. Therefore, researchers devoted their efforts to developing new parent adsorbents and composites of advanced adsorption and thermal characteristics. An example of advanced tuneable parent adsorbents is metal-organic frameworks (MOF) of an exceptionally large surface area of up to 5500 m²/g and defined molecular adsorption sites [17,18]. However, despite these qualities, many MOFs are highly unstable, making them problematic to utilise in real-life applications. Besides, MOF's mass production is not financially viable yet [18,19].

Researchers have developed composite adsorbents using metal salts supported by porous materials and graphite derivatives as thermal conductivity enhancers to improve the adsorbents' heat and mass transfer properties. Examples of such composites are calcium chloride/silica gel/expanded graphite, sodium bromide/expanded graphite, calcium chloride/activated carbon with expanded graphite, and Lithium

* Corresponding author.

E-mail address: a.rezk@aston.ac.uk (A. Rezk).

<https://doi.org/10.1016/j.applthermaleng.2023.120631>

Received 18 October 2022; Received in revised form 9 April 2023; Accepted 18 April 2023

Available online 24 April 2023

1359-4311/© 2023 The Author(s). Published by Elsevier Ltd. This is an open access article under the CC BY license (<http://creativecommons.org/licenses/by/4.0/>).

Nomenclature		∇	gradient
C_p	Specific heat capacity [$\text{kJ kg}^{-1} \text{K}^{-1}$]	τ^{-}	stress tensor [Pa]
H	Enthalpy [kJ kg^{-1}]	<i>Superscripts</i>	
T	Temperature [K]	*	Equilibrium
R	Gas law constant [$\text{kJ kmol}^{-1} \text{K}^{-1}$]	<i>Subscripts</i>	
P	pressure [Pa]	a	activation
K	Thermal conductivity [$\text{W m}^{-1} \text{K}^{-1}$]	l	liquid
K_o	Adsorption constant [KPa^{-1}]	g	gas
t	Time [s]	p	particle
S_m	Mass source term [$\text{kg m}^{-3} \text{s}^{-1}$]	eff	effective
S_h	Heat source term [W m^{-3}]	s	solid
Q_{st}	Heat of adsorption [kJ kg^{-1}]	ref	reference
n, m	Tóth heterogeneity constant	i	initial
W	Uptake [kg kg^{-1}]	f	final
W^*	Equilibrium uptake [kg kg^{-1}]	e	exit
E_a	Activation energy [kJ mol^{-1}]	ad	adsorbent
j	Mass flux [kg m^{-2}]	hw	heating water
D	Diameter [m]	cw	cooling water
M	Mass [kg]	chw	chilled water
ΔU	Change in internal energy [$\text{kJ/kg}^\circ\text{C}$]	in	inlet
Q	Heat transmitted [J]	out	outlet
<i>Greek</i>		sat	saturation
μ	Dynamic viscosity [Pa s]	eva	evaporator
ρ	Density [kg m^{-3}]	c	condenser
γ	Porosity [–]	ads	adsorption
k_e	Permeability [m^2]	des	desorption
α	Thermal diffusivity [$\text{mm}^2 \text{s}^{-1}$]		

chloride/activated carbon/expanded graphite. The composites showed higher thermal conductivity and adsorption capacity than the sole parent adsorbent [20–24]. Furthermore, expanded graphite greatly enhanced the composites' thermal resistance [25]. Examples of utilising metal additives are blending silica gel adsorbent with aluminium, stainless steel, brass and copper [26]. Although the metal additives enhanced the thermal performance of the blends, a considerable amount of the effective adsorbent materials were replaced by additives that negatively affected the overall adsorption capacity [26,27].

Graphene and its derivatives have recently drawn the researchers' attention due to their advanced thermophysical characteristics, such as a large specific surface area of $2630 \text{ m}^2/\text{g}$ and high thermal conductivity of $3000\text{--}5000 \text{ W/mK}$ [28]. Graphene is a two-dimensional monoatomic sheet of carbon atoms arranged in a hexagonal structure with an sp^2 hybridised orbit. The carbon atoms in graphene are bonded by covalent bonds in a plane, forming monolayer sheets connected by van der Waals forces. Compared to graphite, the latter is a graphene allotrope of several atomic layers [28,29]. Generally, graphene is produced by two methods: the top-down method and the bottom-up method. The top-down method involves graphite's structural breakdown and separating the interlayers to form graphene sheets [29]. The bottom-up method uses chemical vapour synthesis and carbon source gas to synthesise graphene substrate [28,29].

Graphene oxide (GO) is a graphene derivative produced by graphite oxidation using the Hummers method and the exfoliation of graphite oxide into thin sheets by reducing the number of layers [30,31]. GO has uniform pore size, expandable inter-layer spacing, and active oxygen functional groups, such as epoxy, phenolic hydroxyl and carboxylic, on its surface that act as active sites interacting with water vapour molecules. Furthermore, its swift water transport mechanism has attracted interest in utilising it in dehumidification applications [30,31]. Therefore, Lian et al. [19] studied the water adsorption characteristics, which revealed its potential as an exceptional desiccant with a high water

capacity, up to $0.58 g_w/g_{GO}$ and adsorption kinetics five times higher than silica gel.

Having concluded the above, what is not yet studied is the use of high thermal diffusive parent adsorbents such as graphene oxide to address the poor heat and mass transfer at the material level. Therefore, the critical contribution of this work is to undertake quantitative and qualitative analysis to understand utilising graphene oxide as a parent adsorbent for cooling and desalination and its influence on the system level's energy conversion potential – via exergy analysis – and overall performance – via energy analysis – under various operating conditions. As such, the objectives of this study are (1) Experimentally investigate the adsorption and thermal characteristics of Graphene Oxide and benchmark it against the baseline silica gel adsorbent; (2) develop a 2D Multiphysics computational model to envisage the heat and mass transfer performance at the adsorbent bed level; (3) study the influence of varying the heat source temperature, cycle time and evaporation temperature on the adsorbent bed and overall system performance by undertaking energy and exergy analyses when utilising graphene oxide and silica gel.

2. Materials and experiments

2.1. Materials

This work investigated GO as a new water sorbent for cooling cum desalination application and benchmarked against the widely used RD Silica gel (RD 2060 of $0.18\text{--}1 \text{ mm}$ particle size) and porosity of 0.36. GO of 1–3 carbon atomic layers and a particle size of $0.5\text{--}20 \mu\text{m}$ was utilised and sourced from Graphitene Ltd. Fig. 1 shows SEM images for the employed GO and silica gel samples.

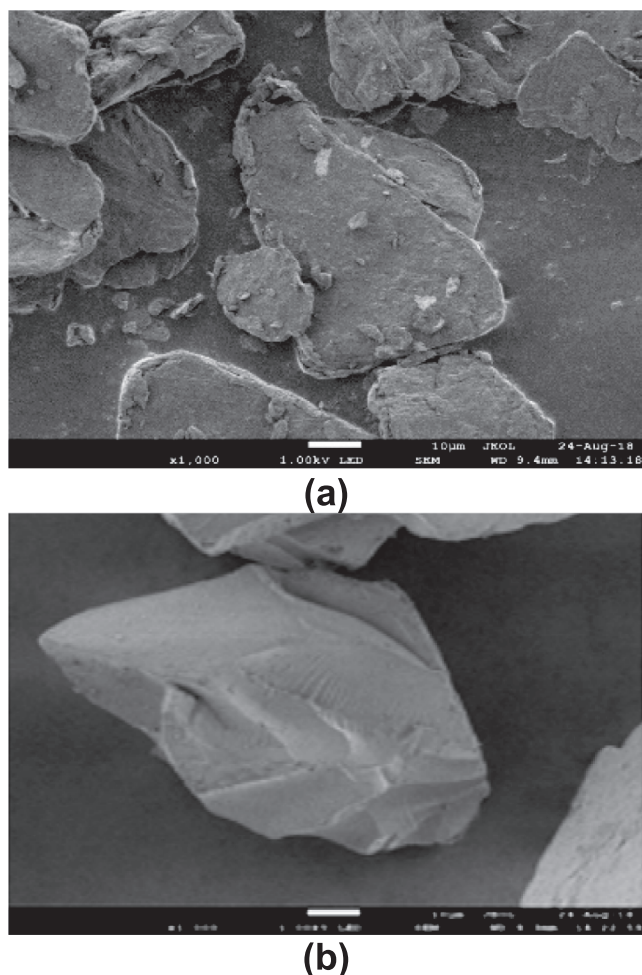


Fig. 1. SEM images for (a) Graphene Oxide and (b) Silica gel.

2.2. Heat transfer characteristics

The bulk thermal diffusivity was experimentally determined using laser flash analyser apparatus (LFA) NETZSCH LFA 467™, schematically

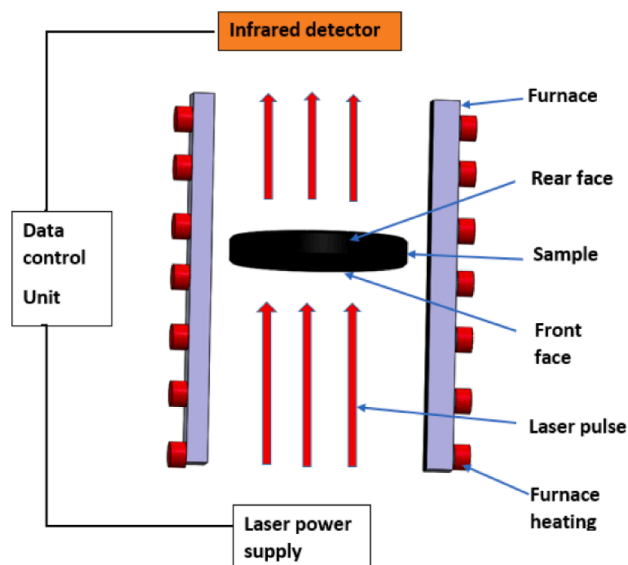


Fig. 2. Schematic diagram of LFA operation.

illustrated in Fig. 2. LFA consists of a laser source, a furnace for temperature control, a sample holder, an infrared detector, and a data control unit. For each measurement, a laser pulse strikes the sample's front face, and the sample's adsorbed heat increases the rear face's temperature. The infrared detector determines the increase in the temperature, and the Data control unit records the measured data. The thermal diffusivity of both GO and SG was measured at a room temperature of 25 °C. The experiments were performed three times with five laser shots at each trial to determine repeatability. The three results show very close values with a standard deviation of 0.01–0.02, giving a repeatability score of 0.005 and 0.01 for GO and SG materials, respectively. The specific heat for GO and SG of 0.734 and 0.921 were utilised to determine their thermal conductivity [32,33]. The rise in temperature at the rear face of the test sample is measured as a function of time and is used to mathematically determine the thermal diffusivity (α) [34]. Eq. (1) was derived by Parker et al. [35] and used for determining the thermal diffusivity.

$$\alpha = 0.1388.l^2/t_{05} \tag{1}$$

where l is the thickness of the sample and t_{05} is the time required for the sample's rear face to reach half the maximum temperature. The sample holder in the apparatus is round and suitable for 12.7 mm diameter samples of thickness in the range of 1–3 mm. Therefore, it was important to maintain the same distance between the IR detector and the reference and test samples to improve the measurement's accuracy. The test and reference samples were coated with graphite to provide the same reflectivity. The test sample thickness in this study was 2.5 mm, the same as a reference sample. The thermal conductivity is then calculated from the thermal diffusivity, specific heat capacity and packing density using Eq. (2).

$$K(T) = \alpha(T) \rho(T) C_p (T) \tag{2}$$

where α is the thermal diffusivity; K is the thermal conductivity; C_p is the Specific heat capacity; ρ is the density of the material; T is the temperature. Table 1 shows the experimentally determined thermal characteristics of GO and SG. On the one hand, the fewer carbon atomic layers of the GO impose an exceptionally high thermal diffusivity feature. On the other hand, oxygen atoms slow the interlayers' heat transfer rate [31]. The thermal diffusivity, therefore, of the GO cumulatively outperformed that of silica gel by 16%.

2.3. Adsorption characteristics

The materials' adsorption characteristics were determined using the dynamic vapour sorption (DVS) gravimetric analyser DVS Resolution™, as shown in Fig. 3. The equipment includes a microbalance (SMS Ultrabalance™) that measures the adsorbent mass to determine the instantaneous water vapour uptake/offtake during adsorption/desorption processes while varying the pressure ratio between the adsorbent and water vapour equivalent to $P_{\text{evap}}/P_{\text{bed}}$. The accuracy of the DVS analyser microbalance was verified at ± 0.05 mg by using 100 mg standard calibration mass before the test. Dry nitrogen purges the reaction and microbalance chambers before every test.

The water vapour uptake corresponding to the vapour pressure values that form adsorption isotherms was developed by measuring the adsorbent mass at no change in mass at a defined water vapour pressure ratio and adsorption temperature. Fig. 4 shows the adsorption isotherms

Table 1
Experimentally measured thermo-physical properties of investigated materials.

Material	Thermal diffusivity [mm ² /s]	Specific heat [Jkg ⁻¹ K ⁻¹]	Thermal conductivity [W/m/K]
GO	0.441	734	1.681
Silica Gel	0.303	921	0.198

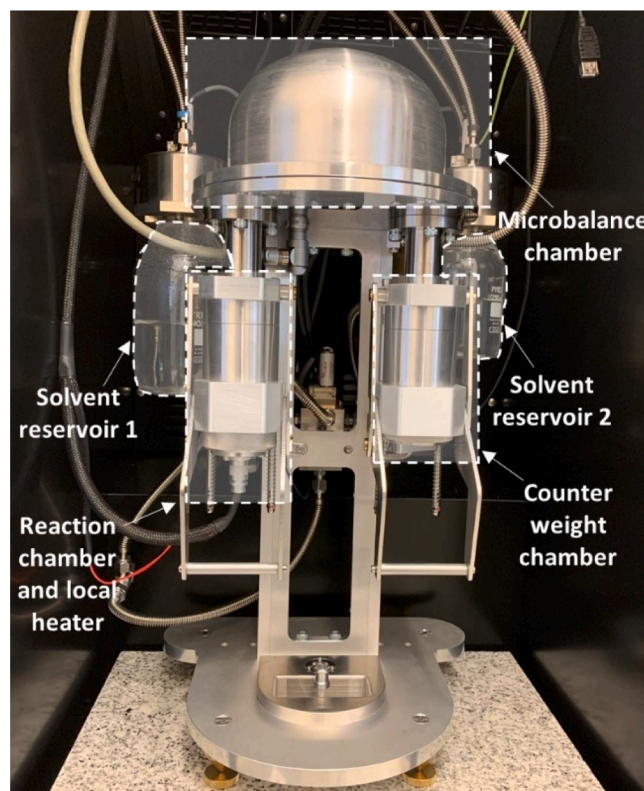
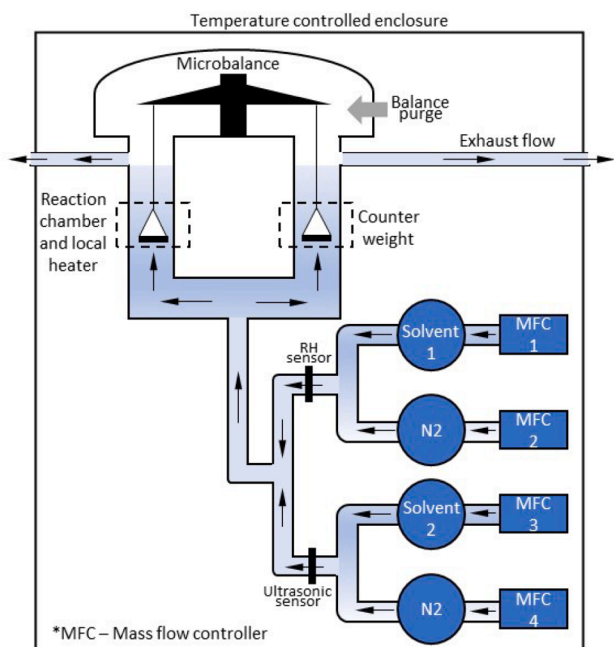


Fig. 3. Dynamic Vapor Sorption Analyser (a) schematic diagram and (b) pictorial view.

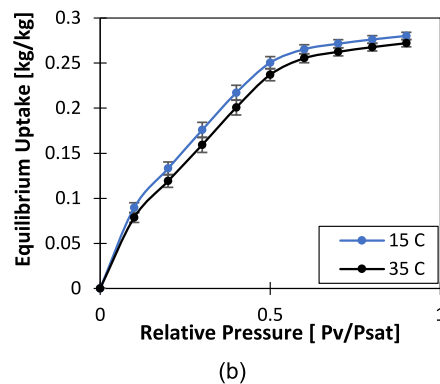
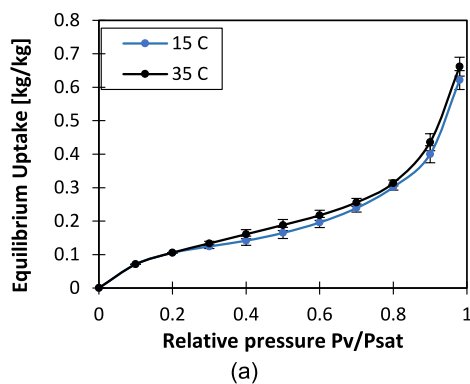


Fig. 4. Experimental isotherms for(a)graphene oxide and(b) silica gel at 15 °C and 35 °C.

of GO and SG measured at 15 and 35 °C. It can be observed that the sorption equilibrium uptake for GO increased by increasing the temperature indicating the chemisorption phenomenon, unlike that for silica gel, decreased by increasing the temperature due to the physical sorption [36].

3. Adsorption characteristics modelling

3.1. Isotherms modelling

Several empirical isotherm models are available to determine the isotherms primarily based on the heat of adsorption, solid saturation loading (i.e., amount of loading to create a monolayer coverage per unit volume of the packing media), adsorption equilibrium constant and temperature-dependent saturation [37–41]. Such models include Henry, Langmuir, Freundlich, Sips, Dubinin-Astakhov, Tóth, Temkin and Hill-

de Boer [37]. However, the Tóth model was the most suitable for mathematically imitating the experimentally determined isotherms for GO, especially at low vapour pressure isotherms. Therefore, Eq. (32) was empirically developed to model GO based on the Tóth equation, dubbed the GO-modified Tóth model.

$$W^* = \frac{K_o \times \exp\left(\frac{Q_{st}}{RT}\right) \times \frac{P_v}{P_{sat}}}{1 + \left[\frac{\exp\left(\frac{Q_{st}}{RT}\right)}{q_m} \times \frac{P_v}{P_{sat}}\right]^{(t)} \times 1 - m \times \left(\frac{P_v}{P_{sat}}\right)^n} \quad (3)$$

where W^* (kg_w/kg_{ads}) denotes the equilibrium uptake; K_o (kPa⁻¹) is the adsorption constant; R is the universal gas constant; T (K) is adsorption temperature; P_v (kPa) is the vapour pressure for the adsorbed vapour; P_{sat} (kPa) is the saturation pressure of the adsorbent at the given operating temperature; q_m (kg/kg) is the monolayer adsorption capacity; t , n and m are empirical dimensionless indexes; Q_{st} (kJ/kg) is the heat of

adsorption. The heat of adsorption is estimated by employing the Clausius-Clapeyron Eq. (4) using equilibrium isotherm data for at least three temperatures. Table 2 shows the parameters of the modified-GO Tóth model developed from experimental data with a regression parameter (R^2) of 0.989 and the isosteric heat of adsorption. The developed isotherm model agrees well with the experimental adsorption isotherm of 0.07 mean deviation, as shown in Fig. 5.

$$Q_{st} = -R \frac{\partial(\ln P)}{\partial \frac{1}{T}} \quad (4)$$

The widely known modified Freundlich model was employed to imitate the adsorption isotherms for the Silica gel – baseline adsorbent – as recommended by Youssef et al. [42]. The modified Freundlich model equation can be described by Eqs. (5)–(7), as the constants are furnished in Table 3 Fig. 6 shows the SG isotherm model.

$$w^* = A(T_{ads}) \left[\frac{P_{sat}(T_{ref})}{P_{sat}(T_{ads})} \right]^{B(T_{ads})} \quad (5)$$

$$A(T_{ads}) = A_0 + A_1 T_{ads} + A_2 T_{ads}^2 + A_3 T_{ads}^3 \quad (6)$$

$$B(T_{ads}) = B_0 + B_1 T_{ads} + B_2 T_{ads}^2 + B_3 T_{ads}^3 \quad (7)$$

3.2. Adsorption kinetics modelling

The adsorption kinetics determine the rate of adsorption and desorption. The linear driving force (LDF) model is widely used and was accepted for governing the adsorption kinetics for GO and SG, as shown in Eq. (8) [43].

$$\frac{\partial \omega}{\partial t} = k_s \alpha_v (w^* - w) \quad (8)$$

$$k_s \alpha_v = 15 \frac{D_s}{R_p^2} \quad (9)$$

$$D_s = D_{so} \exp\left(-\frac{E_a}{RT}\right) \quad (10)$$

Eq. (10), Arrhenius equation, can be rearranged as shown in Eq. (11).

$$\ln D_s = \ln D_{so} - \frac{E_a}{RT} \quad (11)$$

Where $k_s \alpha_v$ is the diffusion time constant: The equilibrium uptake w^* (kg/kg) is determined from the modified Tóth and modified Freundlich models for GO and SG, respectively: w is the uptake at any given time; D_{so} ($m^2 s^{-1}$) is the pre-exponential coefficient; E_a (kJ/kg) is the activation energy; R ($kJ \cdot kmol^{-1} K^{-1}$) is the universal gas constant; D_s ($m^2 s^{-1}$) is the surface diffusivity; R_p is the particle radius (m); T (K) is the adsorbent temperature. The constant 15 was used, as reported by Zhang et al. [44] since the adsorbent particles are spherical. As reported by El-sharkawy et al. [45], the values of D_{so} and E_a were determined by the Arrhenius plot in which $\ln D_s$ is plotted against $(1/T)$. The slope of the plot gives $\frac{E_a}{R}$ and the intercept gives the constant D_{so} based on equation on Eq. (9). The LDF model's coefficients are shown in Table 4.

4. Computational modelling

A 2D Multiphysics simulation model was developed to envisage adsorption/desorption in an adsorbent bed utilising GO/water working

Table 2
GO-Modified Tóth model's coefficients.

Q_{st} (kJ/kg)	K_0 (KPa-1)	R (kJ/kg K)	q_m (kg/kg)	t	m	n
2740	0.2476	8.31	0.612	3.7	1.360	2

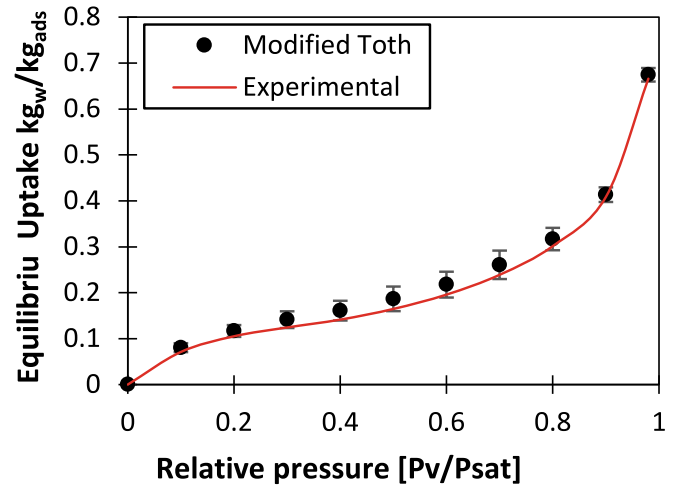


Fig. 5. Isotherms model for GO. modified Tóth.

Table 3
Modified Freundlich model's coefficients.

Constant	Value	Constant	value
A_0	-6.5314	B_0	-15.587
A_1	0.72452E	B_1	0.15915
A_2	-0.23951E-3	B_2	-050612E-3
A_3	0.25493E-6	B_3	0.53290E-6
ΔH_{ads}	2.939E6		

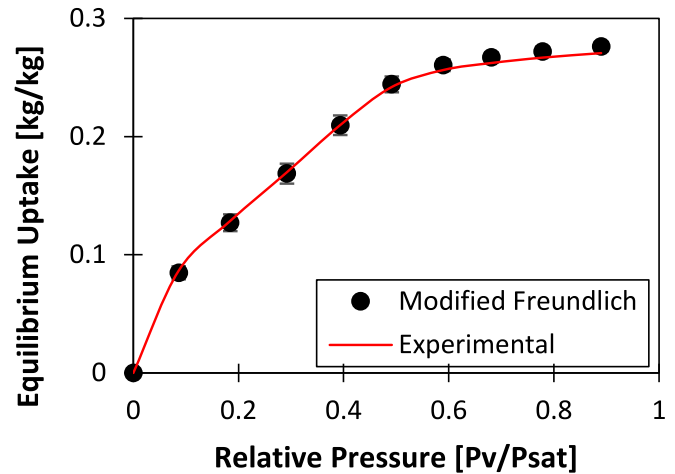


Fig. 6. Isotherm model for SG. modified Freundlich.

Table 4
The empirical constants for the LDF model.

Parameter	value		Unit
	Graphene Oxide	Silica gel	
D_{so}	4.4E-4	2.54E-4	m^2/s
E_a	32,000	42,000	J/mol
R_p	1E-3	0.16E-5	m

pair and benchmark its performance against Silica gel/water. ANSYS Fluent was employed to solve six groups of heat and mass transfer equations. Each group formed a user-defined function (UDF) coupled with the main ANSYS solver to simulate adsorption/desorption processes. The influence of the operating conditions (i.e., temperature and

pressure) on the thermo-physical properties of GO and SG during the adsorption/desorption processes were considered. The simulation procedure is shown in Fig. 7.

4.1. Geometry

The geometry used in the study was a circular finned tube heat exchanger packed with adsorbent materials. Given the symmetry of the heat exchanger, the geometry was reduced to a 2D-axisymmetry model. The computational domain was considered half the space between two fins, as shown in Fig. 8. The dimensions of the geometry are given in Table 5.

4.2. Governing equations

The fundamental physical principles of energy, mass and momentum conservations were used to govern the multi-phase flow of adsorbate in porous media using a finite-volume solver. Jin and Kuznetsov [46] considered the fluid flow in porous media laminar, given the low flow velocity (i.e., low Reynolds number). However, other researchers have used a macroscopic approach for low Reynolds numbers and considered the turbulence effect [47]. In this work, the macroscopic approach was employed to consider any turbulence that might occur in the porous medium.

4.2.1. Adsorbate diffusion

Eq. (12) is the widely used Darcy equation that governs the diffusion process of the adsorbate in finite volume modelling. It models the packed adsorbent material as a block of porous medium [48,49].

$$\frac{\partial}{\partial t}(\rho_w \gamma) + \nabla \left[\rho_w \left(-\frac{k_e}{\mu} \nabla P_{ads} \right) \right] = \frac{\partial}{\partial t}(\rho_{ads} w) \quad (12)$$

where γ is the adsorbent's porosity (m^2/g); μ (Pa.s) is the dynamic

viscosity; ρ_w and ρ_{ads} (kg/m^3) are the densities of water and adsorbent. P_{ads} is the adsorption saturation pressure at the given adsorption temperature; w is water vapour uptake; and k_e (m^2) is the permeability of the adsorbent material. The permeability is a function of the adsorbent particles' radius of the (R_p) and adsorbent porosity, as shown in Eq. (13) [50].

$$k_e = \frac{4\gamma^2 R_p^2}{150(1-\gamma)^2 R_p} \quad (13)$$

4.2.2. Mass conservation equation

Eq. (14) presents the differential form of the Mass conservation equation.

$$\frac{\partial \rho}{\partial t} + \nabla \cdot (\rho \vec{v}) = s_m \quad (14)$$

where S_m ($kg.m^{-3}.s^{-1}$) denotes the mass source term corresponding to the amount of vapour adsorbed onto the adsorbent material porous surfaces, which is governed by Eq. (15).

$$S_m = - (1-\gamma)\rho \frac{\partial \omega}{\partial t} \quad (15)$$

Where the term $\frac{\partial \omega}{\partial t}$ is the adsorption rate of the adsorbate determined from the abovementioned LDF adsorption kinetics model.

4.2.3. The adsorbate mass balance continuity

Eq. (16) governs the continuity of mass of the adsorbate into the porous media during the adsorption/desorption processes.

$$\frac{\partial(\gamma \rho_w)}{\partial t} + \nabla \cdot (\rho_w \vec{v} \gamma) + (1-\gamma)\rho_{ads} \frac{\partial \omega}{\partial t} = 0 \quad (16)$$

The term $\frac{\partial(\gamma \rho_w)}{\partial t}$ denotes the change of density over time in the pores volume; $\nabla \cdot (\rho_w \vec{v})$ is the mass transfer within the adsorbent boundaries; $(1-\gamma)\rho_{ads} \frac{\partial \omega}{\partial t}$ is the unsteady source term of the adsorption process; γ is

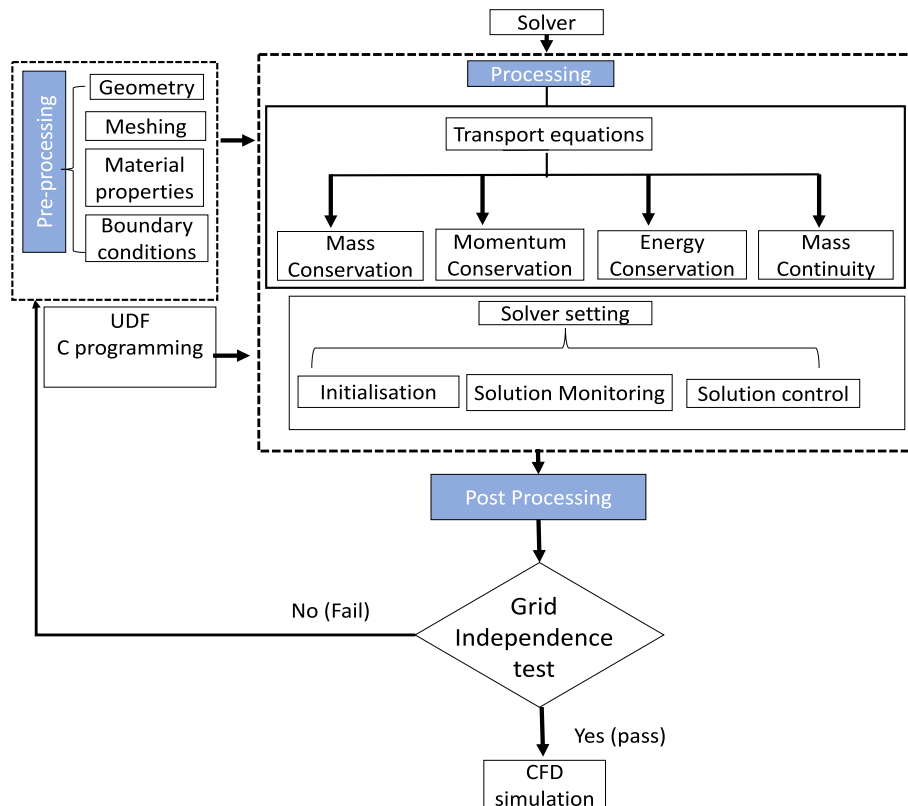


Fig. 7. The simulation procedure.

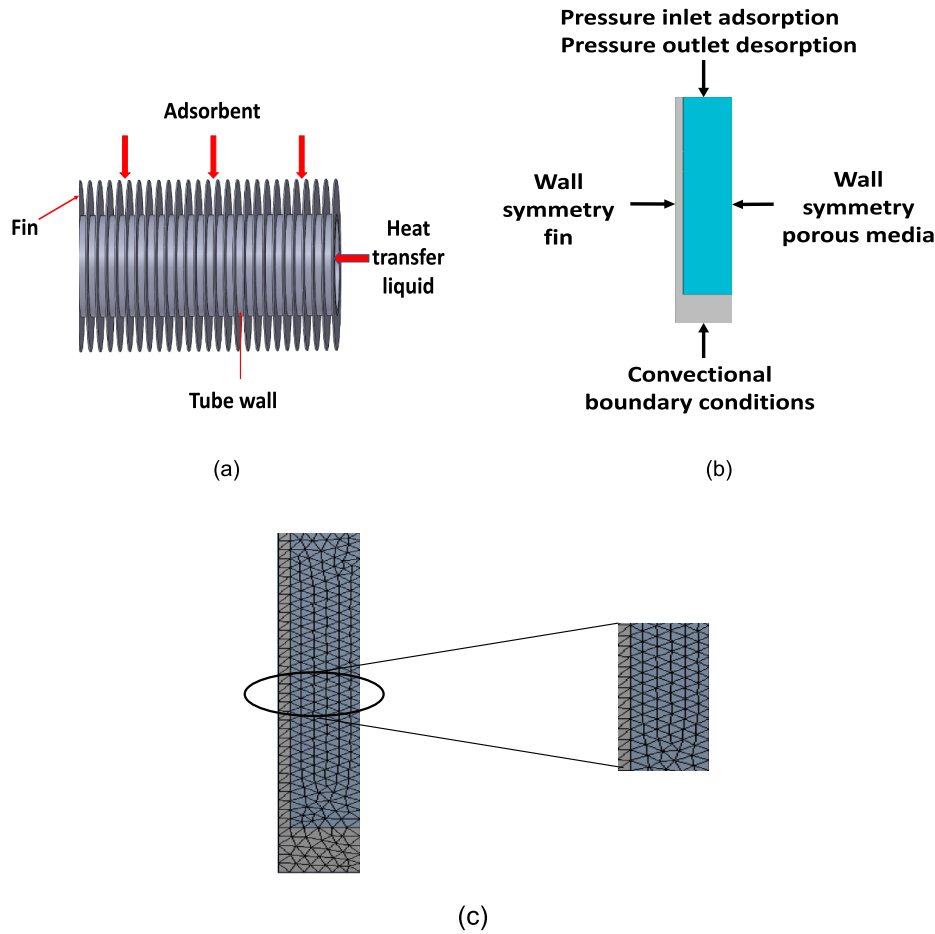


Fig. 8. (a) Simulated geometry, (b) the Axisymmetric segment and (c) mesh.

Table 5
Dimensions of Finned tube for simulation.

Parameter	Value
Tube outer diameter (d_o)	27 mm
Tube inner diameter (d_i)	24 mm
Fin height (h_f)	10 mm
Fin thickness (δ)	0.54 mm
Fin pitch (p)	3.8 mm
length of the finned tube (l)	500 mm

the porosity of the adsorbent bed.

4.2.4. Momentum conservation

The porous media model (PMM) was chosen to simulate the flow in the adsorbent material within ANSYS Fluent platform, which considers the flow resistance in the porous medium. The viscous and inertial losses in the porous medium are accounted for by the momentum source term (F) in Eq. (17).

$$\frac{\partial}{\partial t}(\rho_w \vec{v}) + \nabla \cdot (\rho \vec{v} \vec{v}) = -\nabla p + \nabla \cdot (\vec{\tau}) + \rho_w \vec{g} + \vec{F} \quad (17)$$

Where, ρ_w (kg/m³) denotes the density of adsorbate; \vec{v} (m.s⁻¹) is the velocity vector; $\rho \vec{g}$ (N) the gravitational forces [51].

4.2.5. Energy conservation

Eq. (18) is the general form of energy conservation, assuming the thermal equilibrium between the fluid and the porous medium [7].

$$\frac{\partial}{\partial t}(\rho_w E) + \nabla \cdot (v(\rho_w U + p)) = \nabla \cdot (K_{eff} \nabla T - \sum hJ) + \nabla \cdot (\vec{\tau} \cdot \vec{v}) + S_h \quad (18)$$

where K_{eff} (W/mK) denotes the effective thermal conductivity of the adsorbent; h (J/kg) is the enthalpy of adsorption, J (kgm⁻¹) is the diffusion flux; U (kJ) is the internal energy obtained from $E = h - p/\rho + v^2/2$; $\nabla \cdot (K_{eff} \nabla T)$ is the energy transfer by conduction in the porous medium; $\sum hJ$ is the diffusion flux; $\nabla \cdot (\vec{\tau} \cdot \vec{v})$ is the viscous dissipation; S_h (Wm⁻³) is the heat source term that correlates to the heat of adsorption (Q_s) during the adsorption/desorption process [43]. The energy source term is determined using Eq. (19).

$$Sh = -(1 - \gamma)\rho Q_s t \frac{\partial \omega}{\partial t} \quad (19)$$

4.2.6. Computational grid

A computational mesh was developed to replicate the computational domain, which was bounded by the pressure inlet, fin wall symmetry, porous medium's wall symmetry and tube wall. The tetrahedral mesh was employed, which showed a good balance between simulation accuracy and computational time. The water vapour flow in the adsorbent bed was considered laminar flow, which required fine near-wall meshing by the fin to resolve the near-wall domain and reduce the y^+ values. The mesh quality was determined by mesh orthogonality and skewness. The minimum orthogonality observed from the mesh was 0.9999. The orthogonality value is assessed on a scale from 0 to 1, with values close to zero indicating poor quality. The maximum skewness was 0.242, with values from 0 to 0.25 generally considered reasonable in analogues modelling by Ozen [52]. While the mesh quality was high, the pre-processing step can affect a model's convergence and numerical

stability under CFD analysis. Therefore, it was essential to select mesh parameters that give reliable results and reduce mesh-induced errors, as reported by Sosnowski et al. [53]. This study used the grid convergence index (GCI) method to scrutinise mesh independency. The Fluids Engineering Division of the American Society of Mechanical Engineers recommends the GCI method. It requires analysing the CFD results of the same case at least 3 three times with different mesh resolutions. The first mesh generated was a coarse mesh followed by two refined meshes using a scaling factor of 0.7 and 0.5 using the Eqs. (20)–(25) [53]:

$$h = \left[\frac{1}{N} \sum_{i=1}^N (\Delta A_i) \right]^{\frac{1}{3}} \quad (20)$$

Where N is the total number of cells in the computational domain; ΔA_i is the area of the i^{th} cell. The calculation of the mesh refinement factor (r) was performed as a quotient of the size of coarse and fine mesh, as in Eq. (21):

$$r = \frac{h_{\text{coarse}}}{h_{\text{fine}}} \quad (21)$$

For the calculation of r, the assumption of $h_1 < h_2 < h_3$ was made, where $r_{21} = \frac{h_2}{h_1}$ and $r_{32} = \frac{h_3}{h_2}$. Accordingly, calculating the order of convergence p was performed using Eqs. (22)–(24). Employing the fixed-point iteration with the initial approximation equal to the first term:

$$p = \frac{\left| \ln \left| \frac{\epsilon_{32}}{\epsilon_{21}} \right| + \ln \left(\frac{r_{21}^p - 1 \cdot \text{sgn} \left(\frac{\epsilon_{32}}{\epsilon_{21}} \right)}{r_{32}^p - 1 \cdot \text{sgn} \left(\frac{\epsilon_{32}}{\epsilon_{21}} \right)} \right) \right|}{\ln(r_{21})} \quad (22)$$

$$\epsilon_{32} = \phi_3 - \phi_2 \quad (23)$$

$$\epsilon_{21} = \phi_2 - \phi_1 \quad (24)$$

ϕ_k represents the value of the simulation's most concerned variable, of which a solution is obtained with the k^{th} mesh; the water uptake was the selected variable in this study. The calculation of the extrapolated values was based on Eqs. (25) and (26).

$$\phi_{\text{ext}}^{21} = \frac{r_{21}^p \phi_1 - \phi_2}{r_{21}^p - 1} \quad (25)$$

$$\phi_{\text{ext}}^{32} = \frac{r_{32}^p \phi_2 - \phi_1}{r_{32}^p - 1} \quad (26)$$

The calculation of the approximate relative error was based on Eqs. (27) and (28).

$$e_a^{21} = \left| \frac{\phi_1 - \phi_2}{\phi_1} \right| \quad (27)$$

$$e_a^{32} = \left| \frac{\phi_2 - \phi_3}{\phi_2} \right| \quad (28)$$

Calculating the relative extrapolated errors was based on Eqs. (29) and (30).

$$e_{\text{ext}}^{21} = \left| \frac{\phi_{\text{ext}}^{12} - \phi_1}{\phi_{\text{ext}}^{12}} \right| \quad (29)$$

$$e_{\text{ext}}^{32} = \left| \frac{\phi_{\text{ext}}^{23} - \phi_2}{\phi_{\text{ext}}^{23}} \right| \quad (30)$$

The mesh convergence index GCI calculation was based on Eqs. (31)

and (32).

$$GCI_{21} = \frac{1.25 \cdot e_a^{21}}{r_{21}^p - 1} \quad (31)$$

$$GCI_{32} = \frac{1.25 \cdot e_a^{32}}{r_{32}^p - 1} \quad (32)$$

The convergence type was evaluated using Eq. (33)

$$\frac{\epsilon_{\text{course}}}{\epsilon_{\text{fine}}} = \begin{cases} < 0 & \text{Oscillatory converged} \\ > 1 & \text{not converged} \\ [0.1] & \text{converged} \end{cases} \quad (33)$$

The mesh parameters and values calculated with Eqs. (20)–(32) are in Table 6. The obtained mesh independency study showed a mesh convergence with a GCI of 0.54%.

4.2.7. Boundary conditions

The finned tube walls and the adsorbent domains have matching surfaces with different mesh topologies, and an interface was created (region-src.) to exchange heat between them numerically. The no-slip boundary condition was imposed between the adsorbent and the finned tube walls. The water vapour flow to the adsorbent is a function of the pressure and temperature. Accordingly, the pressure inlet was the most suitable boundary condition at the interface between the porous medium and the surrounding water vapour.

Convection heat transfer occurs between heating/cooling water and the inner tube walls. The calculated heating/cooling water flow rate to maintain adsorption and desorption temperature was 0.036 kg/s. The heat transfer coefficient for the convection heat transfer was determined using Dittus and Boelter correlation, as shown in Eq. (34), and imported into the solver as a parameter in the thermal boundary conditions [54]. Computationally, the heating and cooling processes assumed no friction or relative movement between the heat transfer fluid layer and the boundary wall.

$$h = \frac{0.023 Re_{Dh}^{0.8} Pr^{0.4} k_f}{D_h} \quad (34)$$

where D_h denotes the hydraulic diameter (m); Re is Reynolds number; Pr is Prandtl number; k_f is the thermal conductivity of the heating/cooling water (i.e., heat transfer fluid).

4.3. Performance assessment

Fig. 10 shows the adsorption system considered to determine the system-level performance. Eqs. (35)–(38) show the specific daily water production (SDWP), specific cooling power (SCP), coefficient of performance (COP) and exergy efficiency (η_{ex}), which were employed to assess the performance of the adsorption system for cooling and desalination applications. Fig. 9 is a schematic diagram of the adsorption cooling and desalination cycle used in this study.

$$SDWP = N \int_0^{t_{\text{cycle}}} \frac{\dot{Q}_c}{\rho_w h_{fg} M_{ad}} dt \quad (35)$$

where t_{cycle} is cycle time; h_{fg} is the latent heat of condensation of water; M_{ad} is the adsorbent mass; ρ_w is density of water 1 tonne /m³; N (day⁻¹) is number of cycles per day defined by $N = 86400[\text{s}/\text{d}]/t_{\text{cycle}}$; \dot{Q}_c (kW) is the condensation heat flux.

$$SCP = \int_0^{t_{\text{cycle}}} \frac{Q_c}{M_{ad}} dt \quad (36)$$

$$COP = \int_0^{t_{\text{cycle}}} \frac{Q_c}{Q_{des}} dt \quad (37)$$

Table 6
The calculated mesh parameters.

N (-)	ϕ (-)	h (-)	r (-)	ϵ (-)	$\epsilon_{course}/\epsilon_{fine}$	P (-)	ϕ_{ext} (-)	e_a (%)	e_{ext} (%)	GCI (%)
714	0.736	0.0025	1.4	-0.36	-	-	-	-	-	-
357	0.7235	0.0035	1.43	-0.1	converged	4.46	0.739	1.17	0.40	0.54
152	0.707	0.0050	-	-	-	-	-	-	-	-

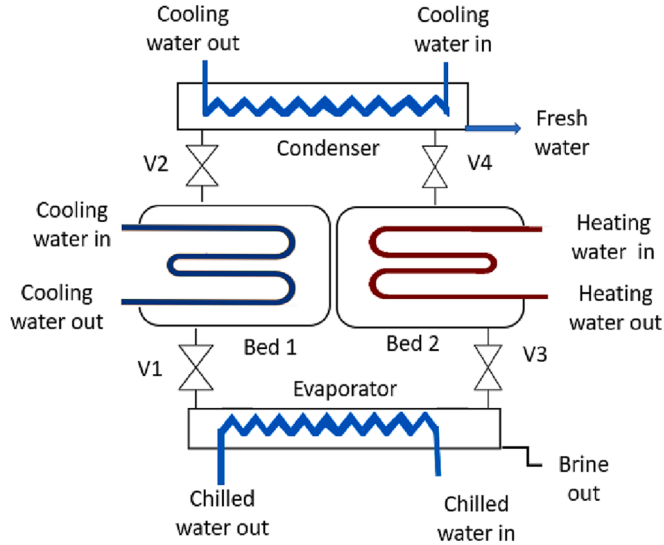


Fig. 9. Schematic diagram of adsorption cooling and desalination system.

$$\eta_{ex} = \frac{\int_0^{t_{cycle}} E_x Q_c dt}{\int_0^{t_{cycle}} E_x Q_{in} dt} \quad (38)$$

The calculation of the Q_c , Q_e , Q_{des} , Q_{in} and E_x are detailed in the supporting information document. It is noteworthy that exergy efficiency is crucial to assess the impact of the entropy generated (i.e., the irreversibility) in the adsorbent bed alongside the energy conversion efficiency determined by the COP. While the COP quantifies the ratio between the produced cooling and the heat supplied, the exergy efficiency determines how much of the applied heat is effectively utilised for producing water and cooling. A low exergy efficiency implies less energy is exploited for the useful production of water and cooling, while larger irreversibility in the form of thermal energy wasted while heating the adsorbent bed metal components and the adsorbent material and becoming more dominant at high regeneration temperatures [55]. Therefore, the heat transfer characteristics are crucial in the system's exergy efficiency.

5. Results and discussion

This section presents the validated Multiphysics 2D simulation model for the adsorbent bed. GO's relatively higher thermal diffusivity and adsorption uptake establishes its promising potential to promote heat and mass transfer at the adsorbent bed level, hence the overall system level. Therefore, the cyclic equilibrium uptake, temperature propagation and dynamic uptake were investigated. Furthermore, the influence of promoting heat and mass transfer on the energy conversion potential was investigated via the exergy analysis. Such analyses developed a fundamental understanding of the influence of the primary operating conditions (cycle time and heat source temperature) on the adsorbent bed and overall cycle performance. In addition, two evaporation temperatures were investigated, 12 °C and 30 °C, where the latter represents the condition of prioritising water desalination over cooling. Qualitatively, the undertaken analyses for the GO were benchmarked against

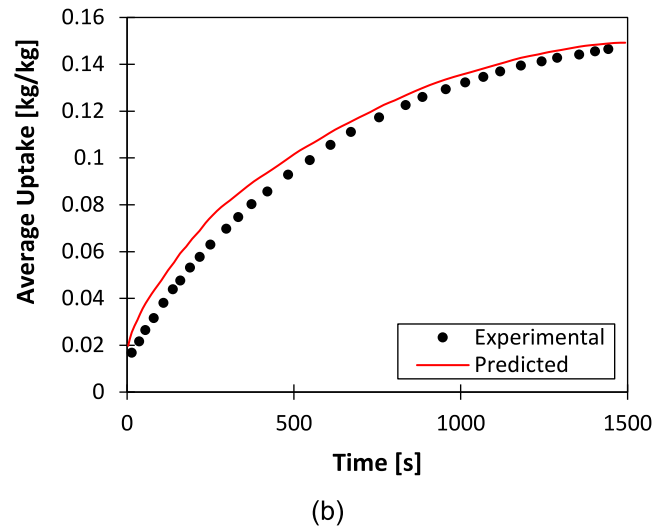
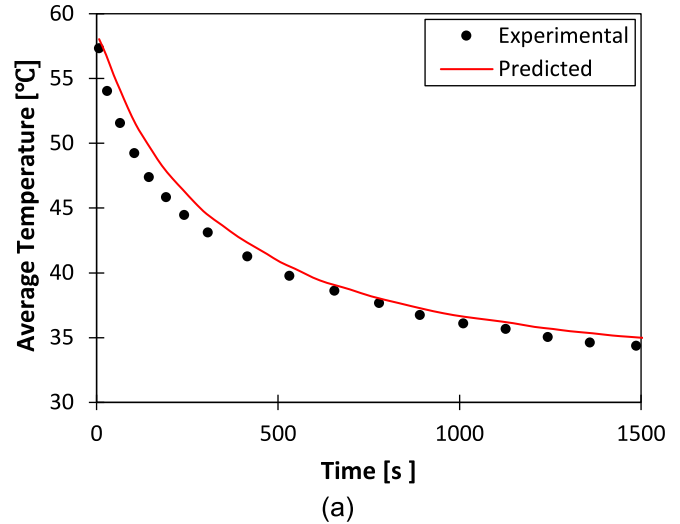


Fig. 10. 2D Multiphysics model validation (a) cyclic temperature profile and (b) cyclic water uptake profile for silica gel/water.

those for the widely used silica gel.

5.1. Modelling validation

Fig. 10 compares the predicted temporal adsorbent bed temperature, water vapour uptake developed from the Multiphysics 2D model and their analogues experimental values obtained from Li et al [56] during an entire silica gel/ water adsorption cycle and the experimental data from Refs. [57,58]. A good agreement between the predicted and experimental data was observed. Therefore, the developed model is deemed acceptable for investigating various adsorption pairs, including GO/water.

5.2. Cyclic performance

The cyclic analysis based on the experimentally developed isotherms

was undertaken to determine the cyclic equilibrium water uptake potential (i.e., the material level figure of merit) for GO and benchmark it against SG, as shown in Fig. 11. In such analysis, the condensation and regeneration temperatures were maintained at 35 °C of 85 °C. At 12 °C evaporator temperature, corresponding to 1 kPa vapour pressure, the net cyclic water vapour uptake was 0.07 kg_w/kg_{ads} for SG and 0.05 kg_w/kg_{ads} for GO water, while 30 °C, corresponding to 4.2 kPa vapour pressure [59], the net cyclic equilibrium uptake of GO outperformed that of SG by 36 %, as the isotherms for both materials' isotherms intersect at 4.2 kPa. It is noteworthy that low evaporator temperature might not be demanded when freshwater production is prioritised over cooling. These findings align with the previously reported results by Lian et al. [19].

The isotherm-based cyclic analysis did not consider the impact of the thermal performance of either material at the adsorbent bed level. Therefore, the Multiphysics model for the adsorbent bed was employed to study the combined effect of adsorption and thermal characteristics for GO and SG at the component level. 800 s cycle time, including 30 s switching (preheating/precooling) time, was considered. Fig. 12 shows the cyclic dynamic changes in the adsorbent bed's temperature at evaporator temperatures 12 °C and 30 °C. Albeit the outstanding performance of silica gel from the isotherm-based cyclic performance

perspective at low evaporator temperature, its low thermal diffusivity hindered the utilisation of such an adsorption capacity. Accordingly, the cyclic uptake of GO outperformed SG at the component level at evaporator temperature below 12 °C by 69.7% over the entire cycle, owing to its relatively faster thermal response, as confirmed by the dynamic temperature profiles in Fig. 12-a and b. The findings align with Elsheniti et al. [2]; the material's low thermal diffusivity negatively impacts the component and system level's performance. At an evaporator temperature of 30 °C, while the cooling water temperature was 35 °C, GO's compound advances in adsorption and thermal characteristics led to higher water uptake by 60 % over the entire cycle, as shown in Fig. 13.

The parameter values and operating conditions used in this study are shown in Table 7.

5.3. Exergy destruction

The exergy analysis was undertaken to understand the degradation of energy in each component during the adsorption/desorption processes using GO/water and SG/water for cooling cum desalination. Table 8 shows the exergy destruction and exergy efficiency for the GO- and SG-based systems. It was observed that the highest exergy destruction occurred in the adsorbent beds. For the investigated operating conditions, the exergy destruction during desorption and adsorption was 9.861 kW and 11.247 kW for the GO-based system at 85 and 30 °C, respectively. The same trend was observed in the SG-based system, as the exergy destruction during the desorption and adsorption were 6.165 kW and 7.523 kW, respectively. These results agree with Cao et al. [60] using the SG/water adsorption pair.

The high exergy destruction in the adsorbent bed is attributed primarily to the substantial temperature differences between the heat transfer fluid and adsorbent at the beginning of the adsorption/desorption processes. These temperature differences comprise most of the irreversibility quantified by the high exergy destruction during the entire cycle. The exergy destruction in desorption is higher than the adsorption due to the relatively higher regeneration temperature level.

The fractional contributions of each component to the overall exergy destruction in the systems are shown in Fig. 14. On the one hand, the GO-based system showed higher exergy destruction, which is attributed to the fact that GO has high thermal diffusivity that increases the heat transfer rate hence higher temperature levels in the adsorbent beds. On the other hand, the same heating water inlet temperature caused the opposite effect in the SG-based system but at the expense of the mass transfer hence the cooling and clean water production. Therefore, the system's exergy efficiency was determined to understand the exergy destruction on the energy conversion quality. As a result, the GO-based system showed a higher overall exergy efficiency of 21.2% than the SG-based system of 16.6%. Such a higher exergy efficiency means more thermal energy was effectively utilised to produce clean water and cooling, which is attributed to GO's superior heat transfer characteristics to SG. In other words, the thermal energy consumed by the metal and the adsorbent material comprises the exergy deficiency in the form of irreversibility [55].

5.4. The effect of cycle time

The effect of cycle time on the adsorbent bed's performance was investigated for two cycles, 800 s and 400 s, including 30 s switching time each and evaporation temperatures of 12 °C and 30 °C, as shown in Figs. 15 and 16. The heating and cooling water inlet temperatures were maintained at 35 °C and 85 °C, respectively. At 400 s cycle time and 30 °C evaporation temperature, the net cyclic water uptake was 0.45 kg_w/kg_{ads} and 0.2 kg_w/kg_{ads} in GO- and SG-based systems. Similarly, at 800 s cycle time, the net cyclic water uptake was 0.57 kg_w/kg_{ads} while SG 0.24 kg_w/kg_{ads} in GO- and SG-based systems, respectively. The higher cyclic water uptake reflects the faster thermal response of GO than SG. At 400 s cycle time and 30 °C evaporation temperature, the net

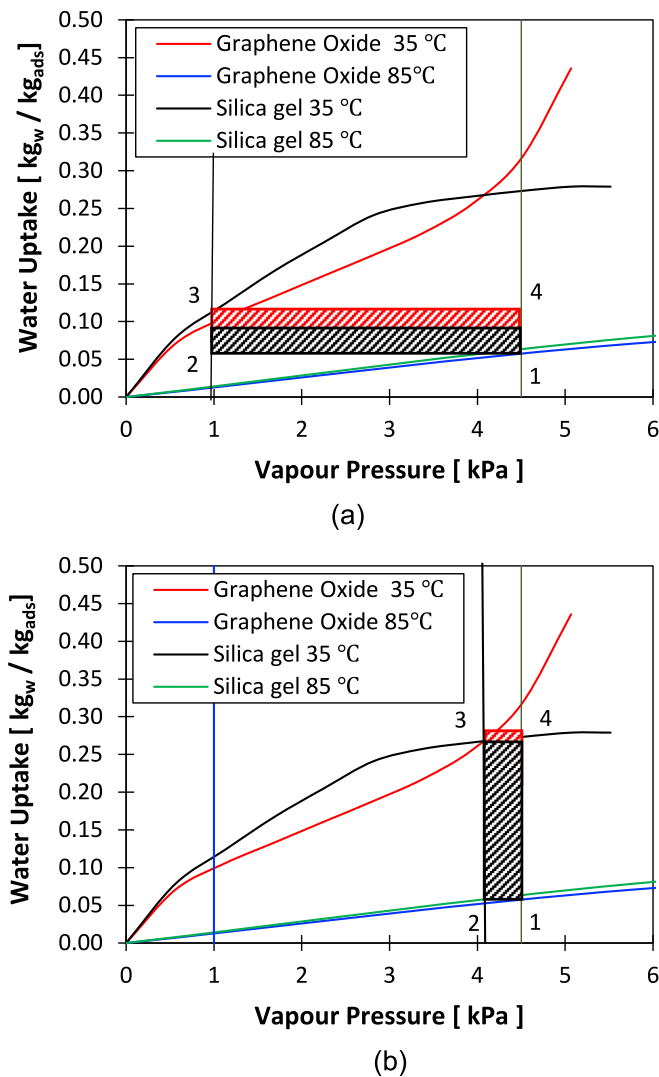


Fig. 11. Comparison of GO and SG at 35 °C, condensation and 85 °C, regeneration temperatures (a) 12 °C evaporation temperature and (b) 30 °C evaporation temperature.

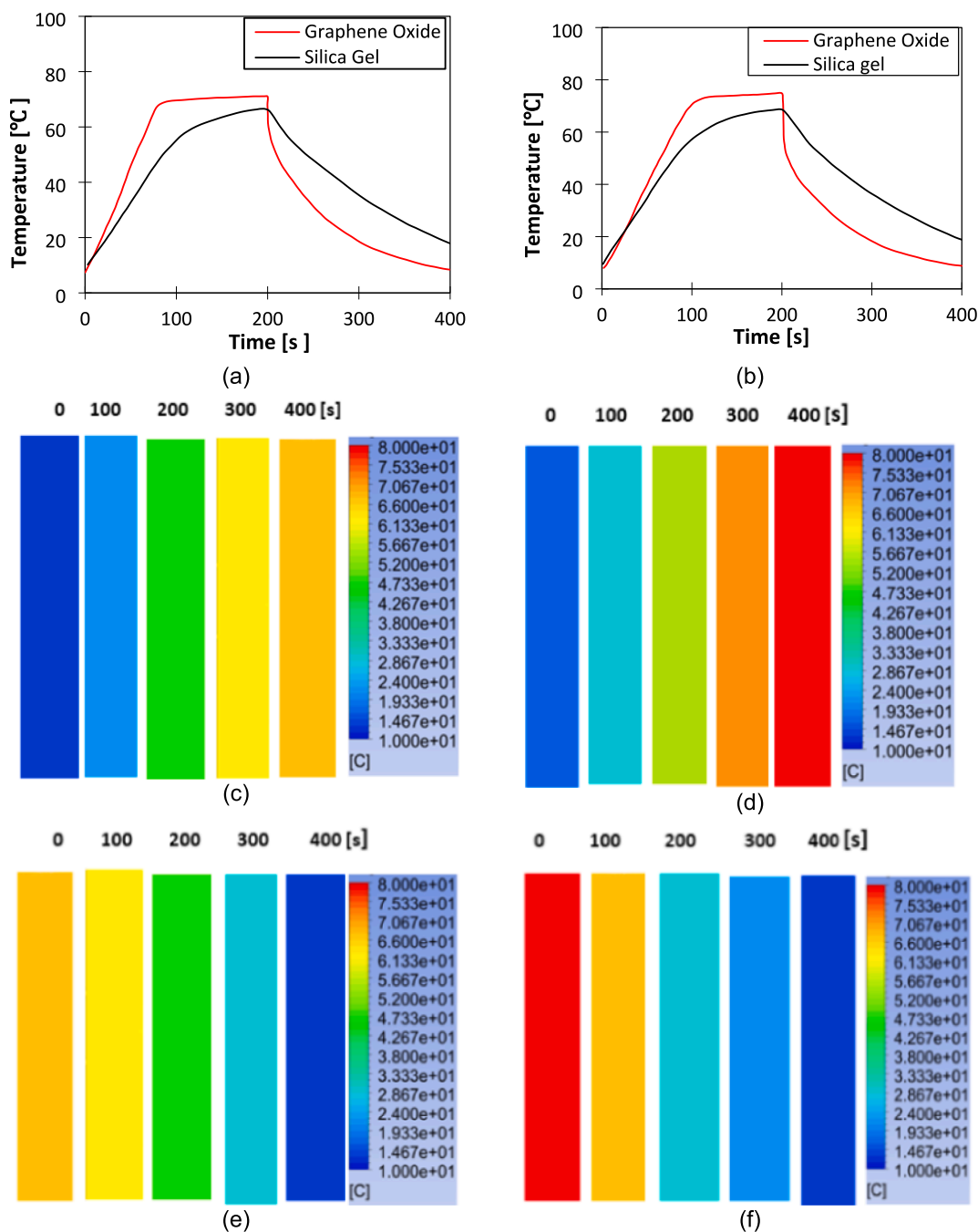


Fig. 12. Dynamic temperature profiles for GO and SG at (a) 12 °C evaporator temperature and (b) 30 °C evaporator temperature; adsorption bed temperature for (c) SG and (d) GO at evaporator temperature 12 °C; (e) desorption bed temperature for (e) SG and (f) GO at evaporator temperature 12 °C.

cyclic temperature rise was 60 °C and 51 °C in GO- and SG-based systems, respectively. At 800 s cycle time, the net cyclic temperature rise was 70 °C and 58 °C in GO- and SG-based systems, respectively. A steep rise in the temperature was observed during the first 100 s and 200 s for 400 s and 800 s cycle times, followed by a plateau in the GO-based system, whereas the temperature rise was gradual in the case of the SG-based system.

At 400 s cycle time and 12 °C evaporation temperature, the net cyclic water uptake was 0.32 kg_w/kg_{ads} and 0.10 kg_w/kg_{ads} in GO- and SG-based systems. At 800 s cycle time, the net cyclic water uptake was 0.352kg_w/kg_{ads} while SG was 0.12 kg_w/kg_{ads} in GO- and SG-based systems. At 400 s cycle time and 12 °C evaporation temperature, the net cyclic temperature rise was 60 °C and 55 °C in GO- and SG-based systems, respectively. At 800 s cycle time, the net cyclic temperature

rise was 71 °C and 57 °C in GO- and SG-based systems, respectively. Similarly, a steep rise was observed in the temperature almost during the first 100 s and 200 s for 400 s and 800 s cycle times, followed by a plateau in the GO-based system. However, the temperature rise was gradual in the case of the SG-based system. The observed plateau in the GO-based system was due to the build-up of heat in the adsorbent bed. During the absorption process, the temperature drop was faster in the first few seconds in the case of the GO-based system than in the SG-based system, followed by a gradual reduction in temperature. Such observation was for the GO-based system under various evaporation temperatures and cycle times. The influence of cycle time observed in this investigation agree with Li et al. [56].

The investigation was extended to include the influence of varying the cycle time on the overall system performance, as shown in

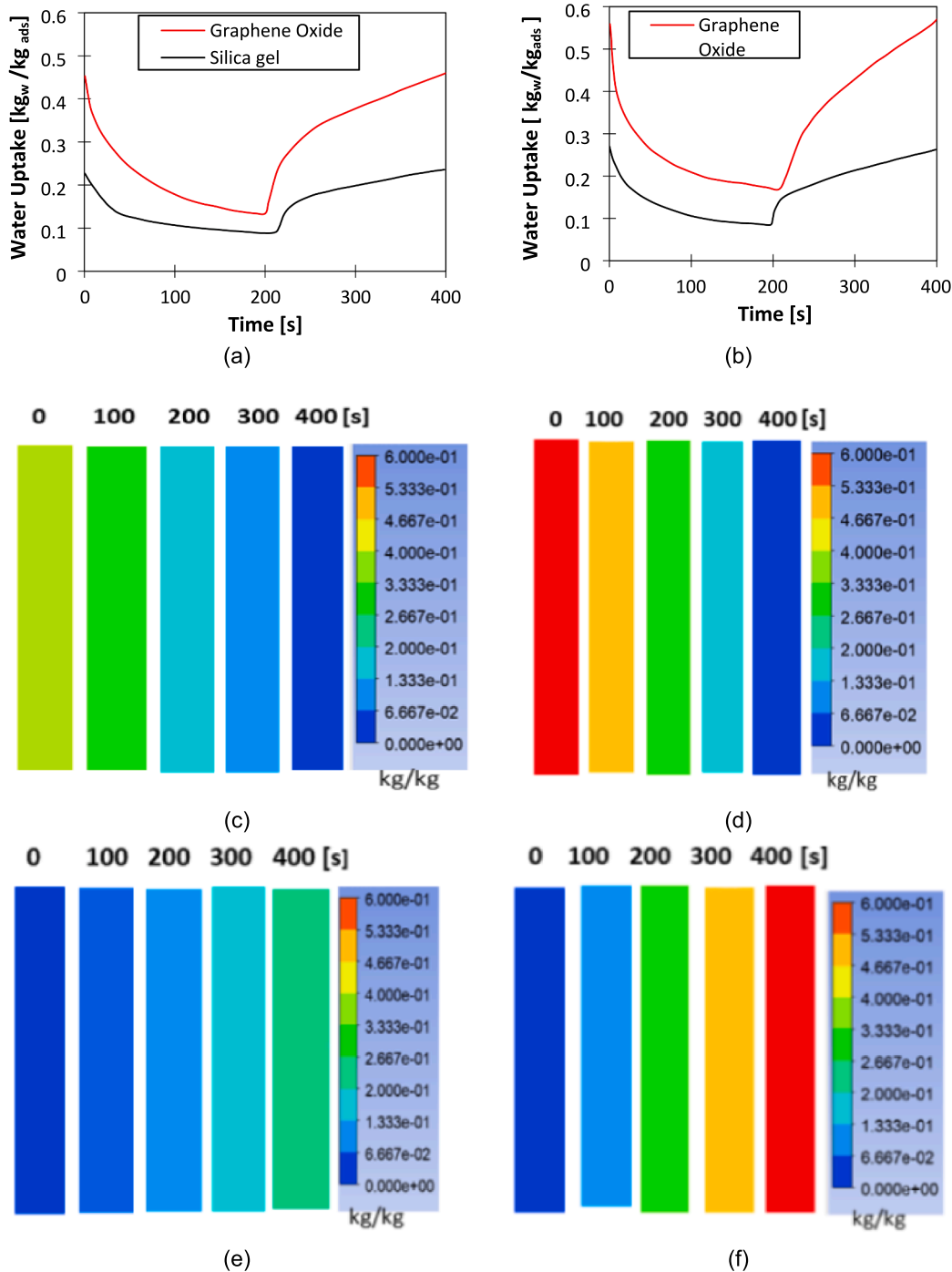


Fig. 13. Dynamic uptake profiles for GO and SG at (a) 12 °C evaporator temperature and (b) 30 °C evaporator temperature; adsorption uptake for (c) SG and (d) GO at evaporator temperature 12 °C; (e) desorption uptake for (e) SG and (f) GO at evaporator temperature 12 °C.

Figs. 17–20. Generally, it was observed that SDWP, SCP, COP, and exergy efficiency in both GO-based and SG-based systems increased by increasing the cycle time as the systems approached the equilibrium conditions. The overall system performance enhancement was attributed to increasing the cyclic water uptake by extending the adsorption/desorption time, which positively influenced the clean water and cooling production. The GO-based system operated at 12 °C evaporation temperature showed SDWP, SCP, COP and exergy efficiency averagely higher than the SG-based system by 46%, 25%, 13 % and 15.8 %. The average increase in SDWP, SCP, COP and exergy efficiency were 41%, 27%, 15% and 19 % when utilising GO compared to SG at 30 °C evaporation temperature. The increase in the overall system performance

reflects a faster thermal response of GO that enhanced the overall cyclic water uptake/offtake hence the water and cooling production. Moreover, the GO-based system’s exergy efficiency outperformed the SG-based system due to the better energy conversion from the heat input to producing cooling and clean water, as mentioned above. **Fig. 15** shows that GO has a higher thermal response resulting in higher temperatures attained during desorption than SG using the existing finned tube heat exchanger (HE). However, using different HE designs might develop different heat transfer profiles, better utilising GO, improving the desorption process and hence the overall system performance (e.g., cooling and water production).

The effect of increasing the cycle time on SDWP and SCP was more

Table 7
Parameters and operating conditions.

Parameter	Value	Unit
M _{GO}	0.4	kg
M _{SG}	0.22	kg
M _{hex}	2.02	kg
T _{evap}	12–30	°C
T _{cond}	35	°C
T _{cw}	35	°C
T _{des}	65–85	°C
T _{ads}	35	°C
T _{chw}	35	°C
Ads/des bed flow rate	0.036	kg/s
Evap flow rate	0.018	kg/s
Cond flow rat	0.048	kg/s
Cycle time	400–800	s

Table 8
Exergy destruction for adsorption system components.

Component/Process	Graphene Oxide	Silica Gel
	Exergy destruction (kW)	
Adsorption at 35 °C	9.861	6.165
Desorption at 85 °C	11.247	7.523
Condenser at 35 °C	1.223	1.202
Evaporator at 30 °C	1.475	1.385
System overall	22.264	14.099
	Exergy efficiency (%)	16.6%

influential in the GO-based system than in the SG-based system at evaporation temperatures of 12 °C and 30 °C. However, the increase in the cooling and water production was accompanied by an increase in the heat added to the system, which caused almost the same change in the COP of the system. A similar change in the exergy efficiency was observed as a function of the ratio between useful outcomes and heat added to the system. The observed results agree with previous work by Cao and Chung [60], which studied the influence of cycle time on the performance of the silica gel/water adsorption cooling system. The changes in the system performance by varying the cycle time from 400 s to 800 s and across the investigated range (100–800 s) are quantified and summarised in Table 9.

5.5. Effect of heat source temperature

In this investigation, the heat source temperature varied from 65 °C to 85 °C considering evaporation temperatures of 12 °C and 30 °C, while the cooling water temperature, condensation temperature and cycle

time remained 35 °C, 35 °C and 800 s. Fig. 21 shows the effect of increasing heating water temperature on the SDWP. Increasing the heat source temperature from 65 °C to 85 °C increased the SDWP for the GO-based system by 30% (from 6 to 8.6 m³/day/ton) and the SG-based system by 53% (from 3.1 to 6.6 m³/day/ton) at 12 °C evaporation temperature. The same trend was observed for the 30 °C evaporation temperature, as increasing the heating water temperature from 65 °C to 85 °C increased the SDWP for the GO-based system by 77% (from 5.5 to 24.6 m³/day/ton), and SG-based system by 73% (from 5.2 to 19.5 m³/day/ton). The GO-based system showed an average SDWP higher than the SG-based system by 34%.

Fig. 22 shows the effect of increasing heating water temperature on the SCP. In alignment with the SDWP trends, the GO-based system outperformed the SG-based averagely by 27.7% at an evaporator temperature of 12 °C and by 24 % at a 30 °C evaporator temperature, assuring the advancement of the GO-based system for water desalination at high evaporation temperature, as previously investigated. Generally, the better performance of the GO-based system across the investigated temperature range is attributed to the advanced thermal diffusivity, hence the higher thermal response at the component level compared to the SG-based system resulting in a higher cyclic water uptake/offtake rate at the system level. Increasing the heat source temperature from 65 °C to 85 °C increased the SCP for the GO-based system by 87.5% (from 17.05 to 137.2 W/kg) and the SG-based system by 87.8% (from 9.2 to 75.47 W/kg) at 12 °C evaporation temperature. Besides, increasing the heating water temperature from 65 °C to 85 °C increased the SDWP for the GO-based system by 30% (from 6 to 8.6 m³/day/ton) and the SG-based system by 43.5% (from 3.13 to 6.6 m³/day/ton). These findings agree with the study by Youssef et al. [42], who investigated the influence of the heating water temperature on the SDWP for the water adsorption desalination system.

Figs. 23 and 24 show the effect of regeneration (i.e., heat source) temperature on the COP and exergy efficiency of the system. Generally, increasing the heat source temperature increased the COP while the exergy efficiency decreased. Although increasing the heat source temperature while maintaining the cooling (i.e., heat sink) temperature increases the cyclic water uptake, cooling, and water production; it increases the heat transferred to the adsorbent bed during the regeneration process. Therefore, increasing the heat source temperature increased the energy conversion efficiency (COP) at the system level within the investigation temperature range. On the other hand, the higher the heat source temperature, the higher the exergy destruction in the desorption bed, which significantly influences the exergy efficiency at the system level causing its decrease.

As a result, the COP for GO increased by 29.5% (from 0.26 to 0.369) and for SG by 30.8% (from 0.173 to 0.25) at 12 °C evaporator temperature, while the increments at 30 °C were 49.4% (from 0.278 to 0.55) for GO and 52.2% (from 0.21 to 0.44) for SG by increasing the heat source

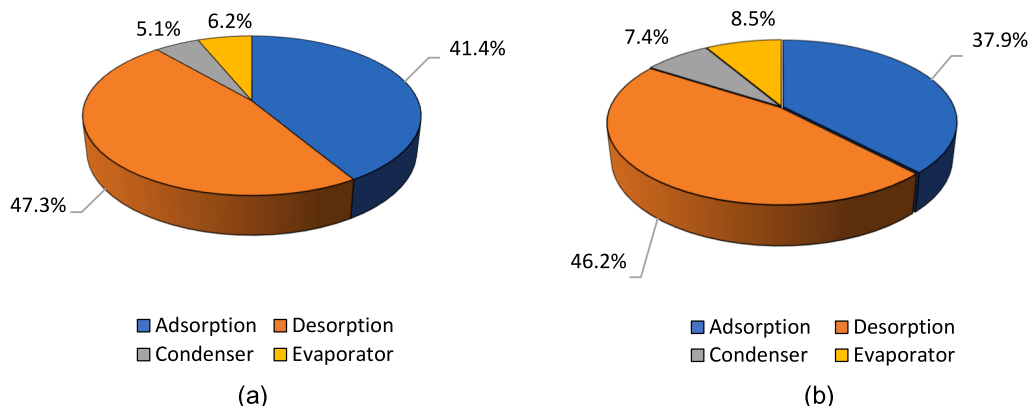


Fig. 14. Exergy destruction fraction for components utilising (a) GO and (b) SG.

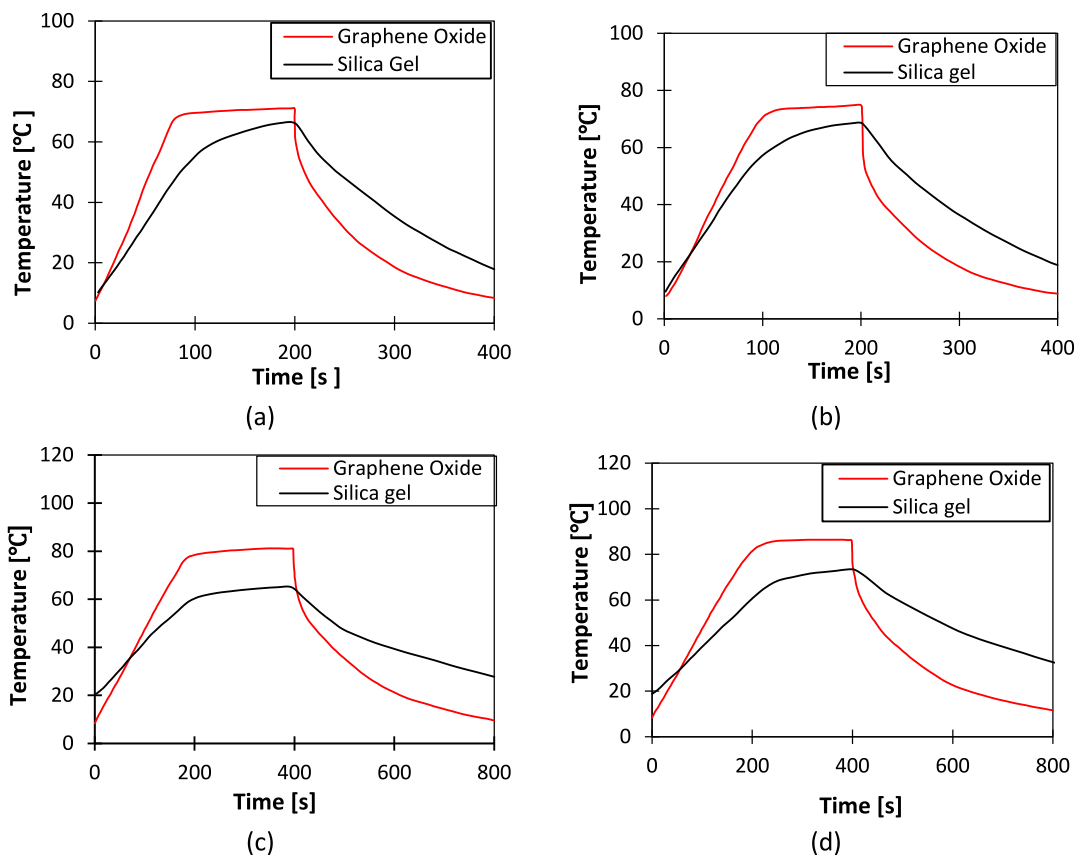


Fig. 15. Dynamic temperature profiles for SG and GO at (a) $T_{ev} = 12\text{ }^{\circ}\text{C}$ temperature $t_{cycle} = 400\text{ s}$; (b) $T_{ev} = 30\text{ }^{\circ}\text{C}$ temperature $t_{cycle} = 400\text{ s}$; (c) $T_{ev} = 12\text{ }^{\circ}\text{C}$ temperature $t_{cycle} = 800\text{ s}$; (d) $T_{ev} = 30\text{ }^{\circ}\text{C}$ temperature $t_{cycle} = 800\text{ s}$.

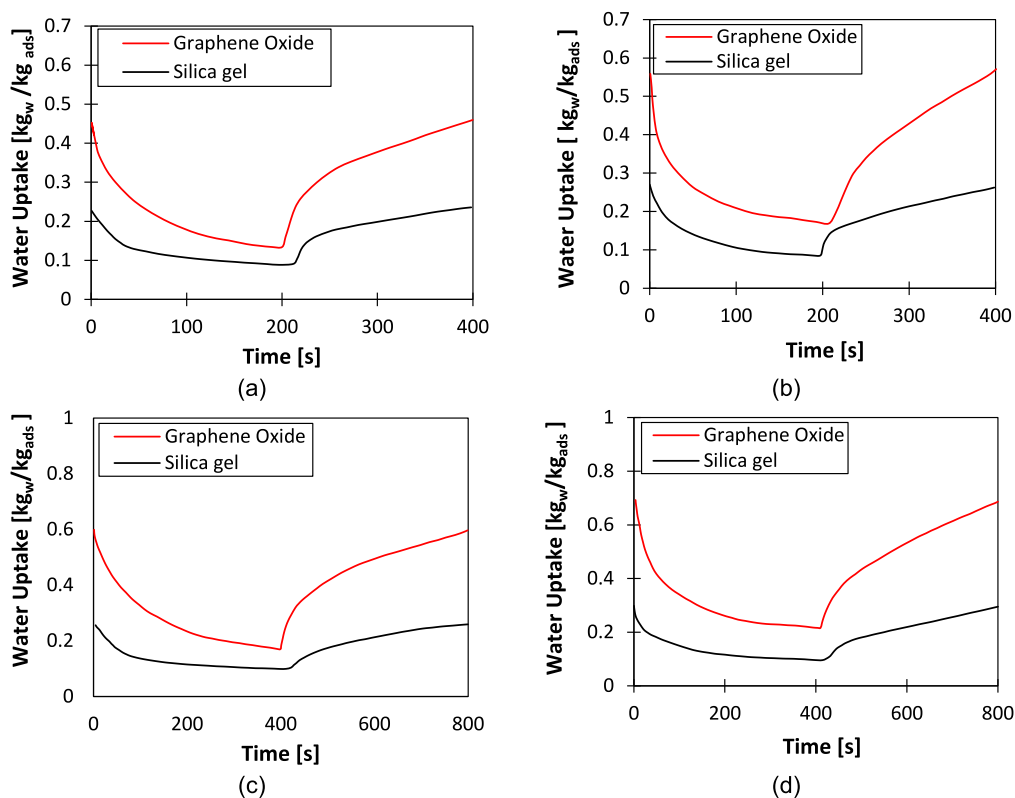


Fig. 16. Dynamic water uptake profiles for SG and GO at (a) $T_{ev} = 12\text{ }^{\circ}\text{C}$ temperature $t_{cycle} = 400\text{ s}$; (b) $T_{ev} = 30\text{ }^{\circ}\text{C}$ temperature $t_{cycle} = 400\text{ s}$; (c) $T_{ev} = 12\text{ }^{\circ}\text{C}$ temperature $t_{cycle} = 800\text{ s}$; (d) $T_{ev} = 30\text{ }^{\circ}\text{C}$ temperature $t_{cycle} = 800\text{ s}$.

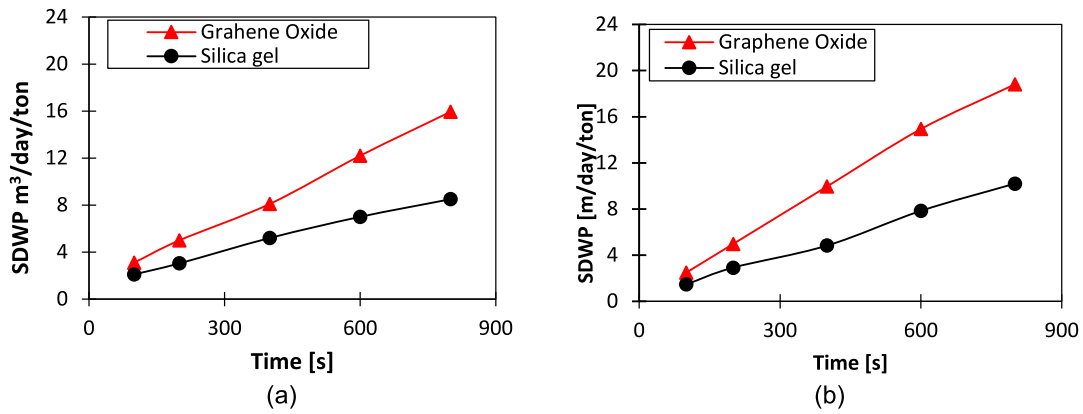


Fig. 17. The effect of changing cycle time on SDWP for GO and SG at (a) $T_{ev} = 12\text{ °C}$ and (b) $T_{ev} = 30\text{ °C}$.

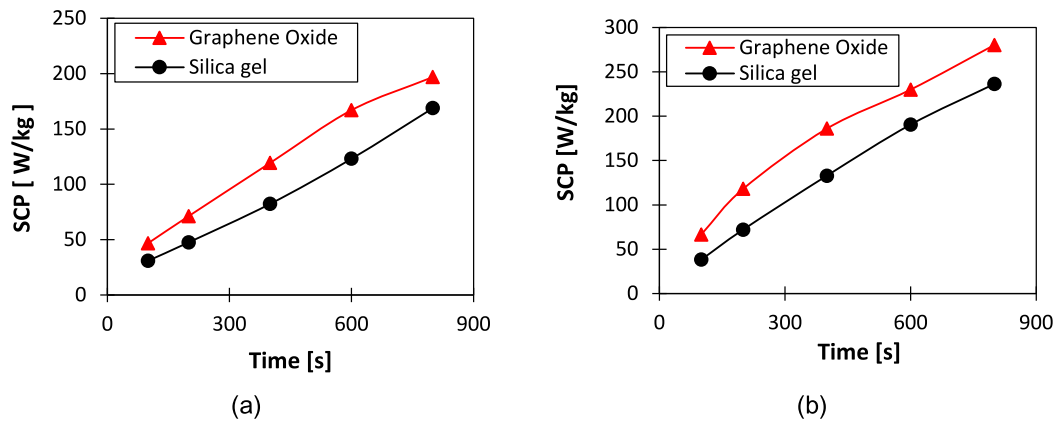


Fig. 18. The effect of changing cycle time on SCP for GO and SG time at (a) $T_{ev} = 12\text{ °C}$ and (b) $T_{ev} = 30\text{ °C}$.

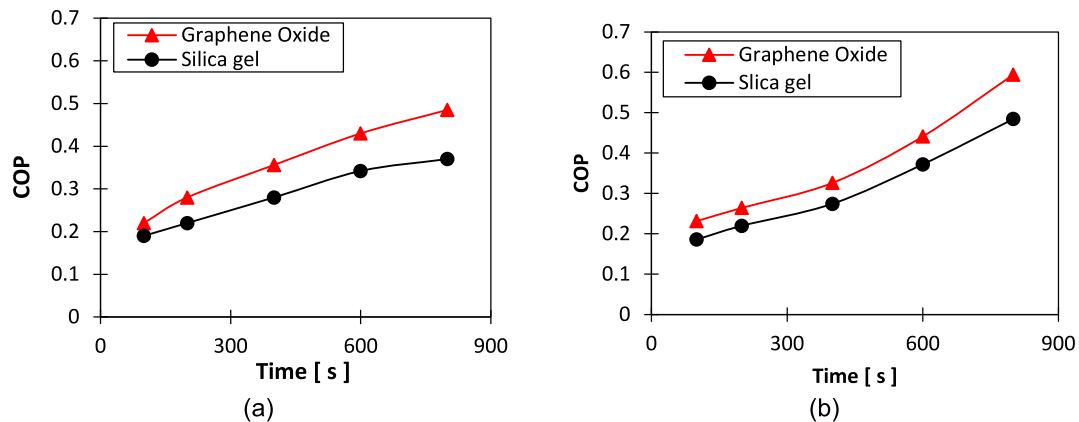


Fig. 19. The effect of changing cycle time on COP for GO and SG time at (a) $T_{ev} = 12\text{ °C}$ and (b) $T_{ev} = 30\text{ °C}$.

temperature from 65 °C to 85 °C, respectively. The exergy efficiency for the GO-based system decreased by 42% (from 0.245 to 0.1402) and for the SG-based system by 44.5% (from 0.218 to 0.121 at 12 °C evaporator temperature, while the increments at 30 °C were 49.2% (from 0.248 to 0.126) for GO and 54.3% (from 0.248 to 0.101) for SG by increasing the heat source temperature from 65 °C to 85 °C, respectively.

The GO's advanced thermal response over SG led the GO-based system to attain higher water cyclic uptake/offtake and higher COP than the SG-based system. It results in COP for the GO-based system being, on average, 32.2 % and 24 % higher than the SG-based system for 12 °C and 30 °C evaporation temperatures. Even though the ratio

between the produced cooling and heat added positively influences the exergy efficiency, increasing the heat source temperature has the opposite effect on the exergy destruction, specifically during the regeneration, which is higher in GO than SG, as previously quantified and demonstrated in Table 6. Such contradicting effects caused the exergy efficiency of the GO-based system averagely outperform that of the SG-based system by 17% and 13.7% for 12 °C and 30 °C evaporation temperatures. Furthermore, the average exergy efficiency increment was lower than the average COP increment by 9.2% and 9.8% for 12 °C and 30 °C evaporation temperatures. The reported results agree with the parametric studies undertaken by Cao and Chung [60] on a silica gel/

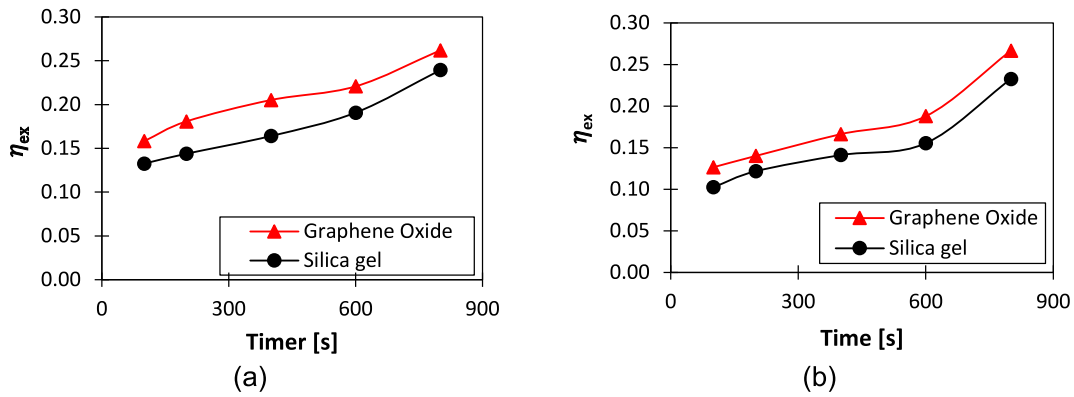


Fig. 20. The effect of changing cycle time on Exergy efficiency for GO and SG time at (a) $T_{ev} = 12\text{ }^{\circ}\text{C}$ and (b) $T_{ev} = 30\text{ }^{\circ}\text{C}$.

Table 9

The percentage change in the system performance by employing GO and SG.

Performance indicator	The material employed and evaporation temperatures				Cycle time change	
	GO		SG		From	To
	$T_{ev} = 12\text{ }^{\circ}\text{C}$	$T_{ev} = 30\text{ }^{\circ}\text{C}$	$T_{ev} = 12\text{ }^{\circ}\text{C}$	$T_{ev} = 30\text{ }^{\circ}\text{C}$		
SDWP [m^3/day ton]	76.3%	75.5%	70%	72%	100 s	800 s
SCP [W/kg]	40.7%	47 %	41%	5.8%	400 s	400 s
COP [-]	76%	76.2%	51.4%	56%	100 s	400 s
η_{ex}	39.4%	52.6%	38.8%	44%	400 s	400 s
	26.5%	45 %	24.3%	43.3%	400 s	400 s
	39.4%	52.5%	44.7%	50.5%	100 s	400 s
	21.4%	37.6%	23.6%	39.3 %	400 s	400 s

water adsorption cooling system.

The SDWP potential of GO as an adsorbent was compared to that achieved by previously investigated adsorbents and is shown in Table 10. Generally, even though the SDWP were obtained from different operating conditions, the achieved SDWP ranged from 4.5 to 24.9 $\text{m}^3/\text{tonne}/\text{day}$. Furthermore, it was observed that GO achieved the second-highest SDWP after Emim-Ac/syloid 72; this indicates the GO's strong potential as an adsorbent, emphasising water desalination application. While graphene oxide exhibited superior adsorption characteristics, it is not widely available in the market and, therefore, it is not the most cost-effective adsorbent. However, the widespread uptake of any new material or technology, such as silica gel and zeolite, leads to large-scale manufacturing at much better value for money. In analogy, wider exploitation of GO will significantly promote its cost-effectiveness.

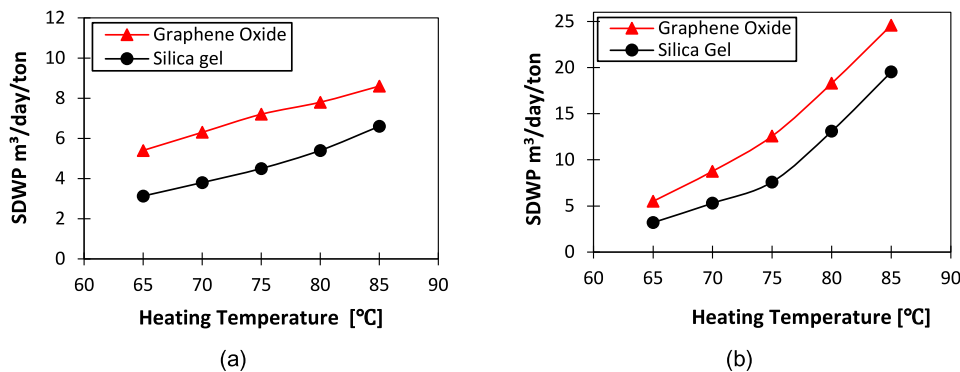


Fig. 21. SDWP at different heating water temperatures at (a) $T_{ev} = 12\text{ }^{\circ}\text{C}$ and (b) $T_{ev} = 25\text{ }^{\circ}\text{C}$.

6. Conclusion and prospects

6.1. Conclusion

This study aimed to undertake quantitative and qualitative analysis on utilising graphene oxide as a parent adsorbent for cooling and desalination and assess its influence on the system level's overall energy conversion potential under various operating conditions. The adsorption and thermal characteristics of graphene oxide were determined and benchmarked against the baseline silica gel adsorbent, which was modelled and coupled with a 2D Multiphysics computational model to envisage the heat and mass transfer performance at the adsorbent bed level. In addition, the influence of varying the heat source temperature, cycle time and evaporation temperature on the adsorbent bed and overall system performance was undertaken via energy and exergy analyses. The key findings of the study are concluded below.

- The high thermal diffusivity of GO significantly influenced the thermal response of the adsorbent bed that advanced the cyclic water uptake at various evaporation temperatures, contradicting the equilibrium uptake cyclic predictions. Despite the faster heat transfer in the GO-based adsorbent bed increased exergy destruction, the exergy efficiency at the system level was availed. As a result, the SDWP, SCP, COP and exergy efficiency for the GO-based system was 40–44.0%, 24.8–29.5%, 14.9–17.2% and 12–15.5% higher than the SG-based system when operated at 12–30 $^{\circ}\text{C}$.
- Increasing the cycle time increased the water uptake in both GO and SG since the adsorbent bed had a longer time to reach closer to equilibrium uptake. As a result, the SDWP, SCP, COP and exergy efficiency for the GO-based system was higher than that of the SG-based system by 40%, 24.8%, 14.9% and 12% at 12 $^{\circ}\text{C}$ evaporation temperature and by 44.4%, 29.5%, 17.2% and 15.5% at 30 $^{\circ}\text{C}$ evaporation temperature. The GO-based system outperformed the

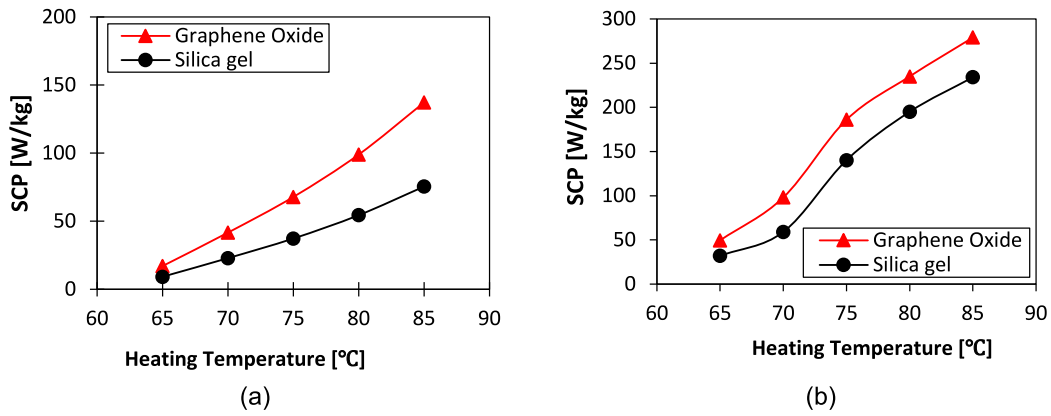


Fig. 22. SCP at different heating temperatures for GO and SG at (a) $T_{ev} = 12$ °C and (b) $T_{ev} = 30$ °C.

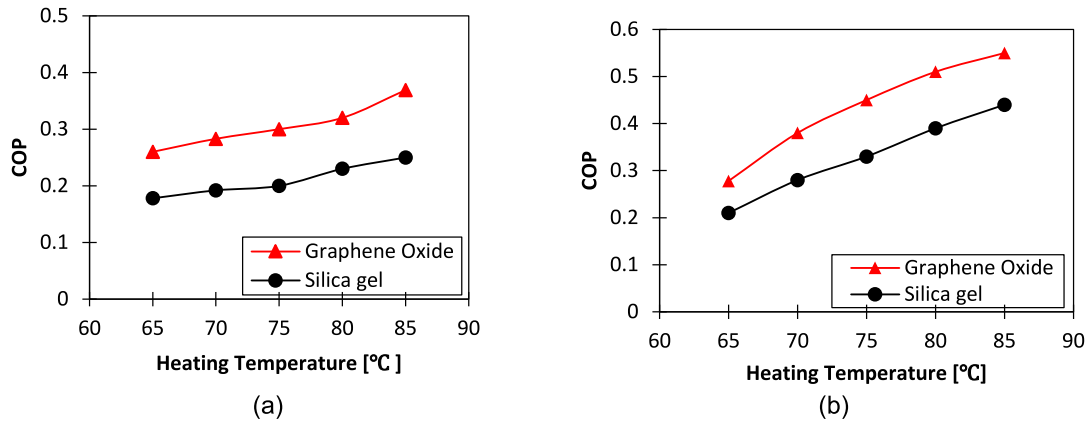


Fig. 23. COP at different heating temperatures for GO and SG at (a) $T_{ev} = 12$ °C and (b) $T_{ev} = 30$ °C.

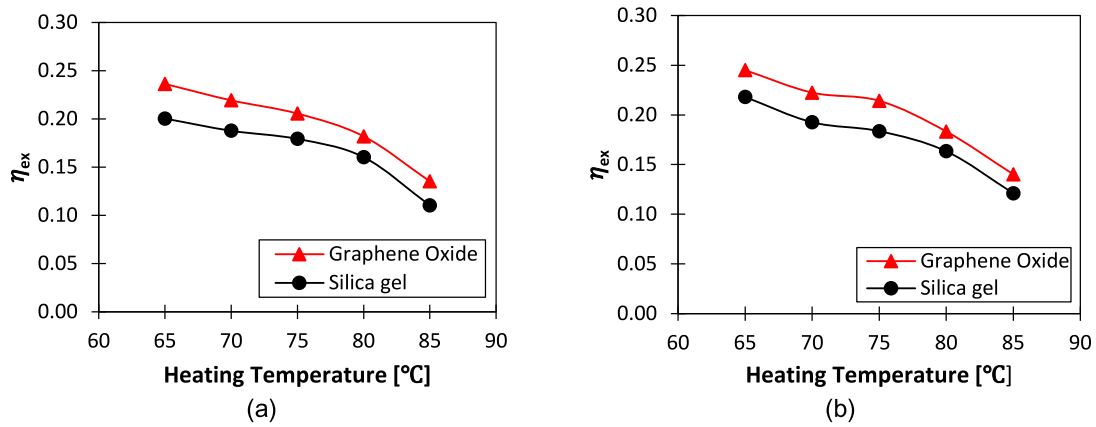


Fig. 24. Exergy efficiency at different heating temperatures for GO and SG at (a) $T_{ev} = 12$ °C and (b) $T_{ev} = 30$ °C.

SG-based system due to a higher thermal response, which led to higher cyclic water uptake.

- Increasing the heat source temperature increased the exergy destruction and reduced exergy efficiency but enhanced the SDWP, SCP and COP. Moreover, the GO-based system’s exergy efficiency was higher than the SG-based system across the investigated heat source temperatures by 13.7% and 17%, on average, at 12 °C and 30 °C evaporation temperatures; this was despite the higher exergy destruction in the former system at the adsorbent bed level.

Overall, having an adsorbent material of advanced thermal diffusivity

is crucial to exploit the advanced adsorption performance at the component and system levels.

6.2. Prospects

This work is a step forward to further research about studying the use of graphene derivatives to enhance the heat and mass transfer at the material level for adsorption systems, such as cooling, desalination and heat storage.

Table 10
SDWP for different types of sorbents presented in the literature.

Adsorbent	Cycle time (s)	SDWP(m ³ /tonne/day)	Application	Ref
Graphene Oxide	800	18.8	Cooling & desalination	This study
Silica gel	300	4.5	Desalination & cooling	[61]
Silica gel RD	–	7.5	Desalination	[62]
Silica gel A+++	1008	10	Desalination & cooling	[63]
AQSOA-ZO2	600	7.4	Desalination	[64]
COP-27 Ni MOF	1440	15	Desalination	[65]
Al fumarate MOF	900	8.2	Desalination & cooling	[66]
Emim-Ac/Syloid 72 FP	600	24.9	Desalination	[67]

CRediT authorship contribution statement

Handsome Banda: Conceptualization, Writing – original draft, Formal analysis, Writing – review & editing. **Ahmed Rezk:** Conceptualization, Writing – review & editing. **Eman Elsayed:** . **Ahmed Askalany:** .

Declaration of Competing Interest

The authors declare that they have no known competing financial interests or personal relationships that could have appeared to influence the work reported in this paper.

Data availability

Data will be made available on request.

Acknowledgement

This work was supported in by The Royal Society (grant no. IES\R3\203128).

Appendix A. Supplementary material

Supplementary data to this article can be found online at <https://doi.org/10.1016/j.applthermaleng.2023.120631>.

References

- [1] S.P. Simonovic, World water dynamics: global modeling of water resources, *J. Environ. Manage.* 66 (3) (2002) 249–267.
- [2] M.B. Elsheniti, et al., Performance of a solar adsorption cooling and desalination system using aluminum fumarate and silica gel, *Appl. Therm. Eng.* 194 (2021), 117116.
- [3] B.B. Saha, et al., Fundamental and application aspects of adsorption cooling and desalination, *Appl. Therm. Eng.* 97 (2016) 68–76.
- [4] I.I. El-Sharkawy, et al., A study on consolidated composite adsorbents for cooling application, *Appl. Therm. Eng.* 98 (2016) 1214–1220.
- [5] B. Choudhury, et al., An overview of developments in adsorption refrigeration systems towards a sustainable way of cooling, *Appl. Energy* 104 (2013) 554–567.
- [6] C.Y. Tso, et al., Experimental performance analysis on an adsorption cooling system using zeolite 13X/CaCl₂ adsorbent with various operation sequences, *Int. J. Heat Mass Transf.* 85 (2015) 343–355.
- [7] L.X. Gong, et al., Experimental study on an adsorption chiller employing lithium chloride in silica gel and methanol, *Int. J. Refrig.* 35 (7) (2012) 1950–1957.
- [8] I.I. El-Sharkawy, et al., Experimental investigation on activated carbon–ethanol pair for solar powered adsorption cooling applications, *Int. J. Refrig.* 31 (8) (2008) 1407–1413.
- [9] S. Bai, et al., Study of the salinity effects on the cooling and desalination performance of an adsorption cooling cum desalination system with a novel composite adsorbent, *Appl. Therm. Eng.* 181 (2020), 115879.
- [10] S. Jribi, et al., CFD simulation and experimental validation of ethanol adsorption onto activated carbon packed heat exchanger, *Int. J. Refrig.* 74 (2017) 345–353.
- [11] M. Shaaban, et al., Performance investigation of adsorption cooling and desalination systems employing thermally enhanced copper foamed bed coated with SAPO-34 and CPO-27 (Ni), *Appl. Therm. Eng.* 205 (2022), 118056.
- [12] S.-Y. Woo, et al., Silica gel-based adsorption cooling cum desalination system: focus on brine salinity, operating pressure, and its effect on performance, *Desalination* 467 (2019) 136–146.
- [13] K. Thu, et al., Performance investigation of a waste heat-driven 3-bed 2-evaporator adsorption cycle for cooling and desalination, *Int. J. Heat Mass Transf.* 101 (2016) 1111–1122.
- [14] E. Elsayed, et al., CPO-27(Ni), aluminium fumarate and MIL-101(Cr) MOF materials for adsorption water desalination, *Desalination* 406 (2017) 25–36.
- [15] R.J.H. Grisel, S.F. Smeding, R.D. Boer, Waste heat driven silica gel/water adsorption cooling in trigeneration, *Appl. Therm. Eng.* 30 (8) (2010) 1039–1046.
- [16] B. Shi et al., Mathematical and CFD modelling for a rectangular finned tube adsorption bed for automotive cooling system, *Proc. of ICAE*, 2013.
- [17] M. Tatlier, Performances of MOF vs. zeolite coatings in adsorption cooling applications, *Appl. Therm. Eng.* 113 (2017) 290–297.
- [18] P. Küsgens, et al., Characterization of metal-organic frameworks by water adsorption, *Micropor. Mesopor. Mater.* 120 (3) (2009) 325–330.
- [19] B. Lian, et al., Extraordinary water adsorption characteristics of graphene oxide. 9 (22) (2018) 5106–5111.
- [20] X. Zheng, et al., Thermal conductivity, pore structure and adsorption performance of compact composite silica gel, *Int. J. Heat Mass Transf.* 68 (2014) 435–443.
- [21] R.G. Oliveira, et al., Novel composite sorbent for resorption systems and for chemisorption air conditioners driven by low generation temperature, *Renew. Energy* 34 (12) (2009) 2757–2764.
- [22] M. Carmona, E. Pérez, M. Palacio, Experimental evaluation of porosity, axial and radial thermal conductivity, of an adsorbent material composed by mixture of activated carbon, expanded graphite and lithium chloride, *Appl. Therm. Eng.* 150 (2019) 456–463.
- [23] K. Fayazmanesh, S. Salari, M. Bahrami, Effective thermal conductivity modeling of consolidated sorption composites containing graphite flakes, *Int. J. Heat Mass Transf.* 115 (2017) 73–79.
- [24] A.A. Askalany, et al., Effect of improving thermal conductivity of the adsorbent on performance of adsorption cooling system, *Appl. Therm. Eng.* 110 (2017) 695–702.
- [25] L.W. Wang, et al., Study of thermal conductivity, permeability, and adsorption performance of consolidated composite activated carbon adsorbent for refrigeration, *Renew. Energy* 36 (8) (2011) 2062–2066.
- [26] H. Demir, M. Mobedi, S.J.i.j.o.r. Ülkü, The use of metal piece additives to enhance heat transfer rate through an unconsolidated adsorbent bed, *Int. J. Refrig.-Rev. Int. DuFroid* 33 (4) (2010) 714–720.
- [27] K.A. Rocky, et al., Recent advances of composite adsorbents for heat transformation applications, *Therm. Sci. Eng. Prog.* 23 (2021), 100900.
- [28] S. Ren, P. Rong, Q. Yu, Preparations, properties and applications of graphene in functional devices: a concise review, *Ceram. Int.* 44 (11) (2018) 11940–11955.
- [29] X.J. Lee, et al., Review on graphene and its derivatives: synthesis methods and potential industrial implementation, *J. Taiwan Inst. Chem. Eng.* 98 (2019) 163–180.
- [30] C. Liu, et al., Recent advance on graphene in heat transfer enhancement of composites, *ES Energy Environ.* 2 (2018) 31–42.
- [31] Y.R. Choi, et al., Role of oxygen functional groups in graphene oxide for reversible room-temperature NO₂ sensing, *Carbon* 91 (2015) 178–187.
- [32] K. Uddin, et al., Specific heat capacities of carbon-based adsorbents for adsorption heat pump application, *Appl. Therm. Eng.* 129 (2018) 117–126.
- [33] H.T. Chua, et al., Adsorption characteristics of silica gel + water systems, *J. Chem. Eng. Data* 47 (5) (2002) 1177–1181.
- [34] I. Jahan, et al., Experimental study on the influence of metal doping on thermophysical properties of porous aluminum fumarate, *Heat Transfer Eng.* 42 (13–14) (2021) 1132–1141.
- [35] W. Parker, R. Jenkins, C. Butler, Flash method of determining thermal diffusivity, heat capacity, and thermal conductivity, *J. Appl. Sci.* 32 (9) (1961) 1679–1684.
- [36] L. Liu, et al., Sorption equilibria, kinetics, and temperature-swing adsorption performance of polyethyleneimine-impregnated silica for post-combustion carbon dioxide capture, *Sep. Purif. Technol.* 266 (2021), 118582.
- [37] K.Y. Foo, B.H. Hameed, Insights into the modeling of adsorption isotherm systems, *Chem. Eng. J.* 156 (1) (2010) 2–10.
- [38] C.-I. Lin, L.-H. Wang, Rate equations and isotherms for two adsorption models, *J. Chin. Inst. Chem. Eng.* 39 (6) (2008) 579–585.
- [39] M. Llano-Restrepo, M.A. Mosquera, Accurate correlation, thermochemistry, and structural interpretation of equilibrium adsorption isotherms of water vapor in zeolite 3A by means of a generalized statistical thermodynamic adsorption model, *Fluid Phase Equilib.* 283 (1) (2009) 73–88.
- [40] F. Stoeckli, T. Jakubov, A. Lavanchy, Water adsorption in active carbons described by the Dubinin-Astakhov equation, *J. Chem. Soc. Faraday Trans.* 90 (5) (1994) 783–786.
- [41] A. Malek, S. Farooq, Comparison of isotherm models for hydrocarbon adsorption on activated carbon, *AIChE J* 42 (11) (1996) 3191–3201.
- [42] P.G. Youssef, S.M. Mahmoud, R.K.J.I.J.o.E. Al-Dadah, Chemical, ecological, geological engineering, effect of evaporator temperature on the performance of water desalination/refrigeration adsorption system using AQSOA-ZO2, *Int. J. Environ. Chem. Ecol. Geol. Eng.* 9 (2015) 679–683.
- [43] M. Khanam, et al., Numerical investigation of small-scale adsorption cooling system performance employing activated carbon-ethanol pair, *Energies* 11 (6) (2018) 1499.

- [44] Y. Zhang, V. Palomba, A. Frazzica, Understanding the effect of materials, design criteria and operational parameters on the adsorption desalination performance – a review, *Energ. Convers. Manage.* 269 (2022), 116072.
- [45] I.I. El-Sharkawy, et al., Adsorption of ethanol onto parent and surface treated activated carbon powders. 73 (2014) 445–455.
- [46] Y. Jin, A.V.J.P.o.F. Kuznetsov, Turbulence modeling for flows in wall bounded porous media: an analysis based on direct numerical simulations, *Phys. Fluids* 29 (4) (2017).
- [47] M. Nimvari, et al., Numerical simulation of turbulent reacting flow in porous media using two macroscopic turbulence models, *Comput. Fluids* 88 (2013) 232–240.
- [48] S. Jiao, Z.J.A.A.M. Xu, Interfaces, Selective gas diffusion in graphene oxides membranes: a molecular dynamics simulations study, *ACS Appl Mater Interfaces* 7 (17) (2015) 9052–9059.
- [49] B. Xia, D.-W.J.C. Sun, E.I. Agriculture, Applications of computational fluid dynamics (CFD) in the food industry: a review, *Comput. Electron. Agric.* 34 (1–3) (2002) 5–24.
- [50] X. Ji, et al., Structure optimization and performance experiments of a solar-powered finned-tube adsorption refrigeration system, *Appl. Energy* 113 (2014) 1293–1300.
- [51] I.I. El-Sharkawy, et al., Adsorption of ethanol onto parent and surface treated activated carbon powders, *Int. J. Heat Mass Transf.* 73 (2014) 445–455.
- [52] M. Ozen, Meshing Workshop, Academia 2014. <https://www.academia.edu/download/51822095/MESHING_WORKSHOP_2014.pdf>.
- [53] M. Sosnowski, J. Krzywanski, R. Scurek, A fuzzy logic approach for the reduction of mesh-induced error in CFD analysis: a case study of an impinging jet, *Entropy* 21 (11) (2019) 1047.
- [54] R.H. Winterton, Where did the Dittus and Boelter equation come from? *Int. J. Heat Mass Transfer* 41 (4–5) (1998) 809–810.
- [55] V. Baiju, C.I.J.o.S.E. Muraleedharan, Energy and exergy analysis of solar hybrid adsorption refrigeration system, *Int. J. Sust. Eng.* 6 (4) (2013) 289–300.
- [56] M. Li, et al., Computational fluid dynamic study on adsorption-based desalination and cooling systems with stepwise porosity distribution, *Desalination* 508 (2021), 115048.
- [57] R.H. Mohammed, et al., Assessment of numerical models in the evaluation of adsorption cooling system performance, *Int. J. Refrig.* 99 (2019) 166–175.
- [58] I.S. Glaznev, Y.I. Aristov, The effect of cycle boundary conditions and adsorbent grain size on the water sorption dynamics in adsorption chillers, *Int. J. Heat Mass Transf.* 53 (9) (2010) 1893–1898.
- [59] G.F.C. Rogers, Y.R. Mayhew, *Thermodynamic and Transport Properties of Fluids*, fifth ed., John Wiley & Sons, 1995.
- [60] N.V. Cao, J.D.J.E.T. Chung, Exergy analysis of adsorption cooling systems based on numerical simulation, *Energ. Technol.* 7 (1) (2019) 153–166.
- [61] X. Wang, K.C. Ng, Experimental investigation of an adsorption desalination plant using low-temperature waste heat, *Appl. Therm. Eng.* 25 (17) (2005) 2780–2789.
- [62] K.C. Ng, et al., Solar-assisted dual-effect adsorption cycle for the production of cooling effect and potable water, *Int. J. Low-Carbon Technol.* 4 (2) (2009) 61–67.
- [63] K. Thu, et al., Performance investigation on a 4-bed adsorption desalination cycle with internal heat recovery scheme, *Desalination* 402 (2017) 88–96.
- [64] P.G. Youssef, S.M. Mahmoud, R.K. Al-Dadah, Performance analysis of four bed adsorption water desalination/refrigeration system, comparison of AQSOA-Z02 to silica-gel, *Desalination* 375 (2015) 100–107.
- [65] P.G. Youssef, et al., Experimental investigation of adsorption water desalination/cooling system using CPO-27Ni MOF, *Desalination* 404 (2017) 192–199.
- [66] E. Elsayed, et al., Experimental testing of aluminium fumarate MOF for adsorption desalination, *Desalination* 475 (2020), 114170.
- [67] A. Askalany, et al., Silica-supported ionic liquids for heat-powered sorption desalination, *ACS Appl. Mater. Interfaces* 11 (40) (2019) 36497–36505.